Journal of Geochemical Exploration 198 (2019) 82–99

Contents lists available at ScienceDirect

Journal of Geochemical Exploration

journal homepage: www.elsevier.com/locate/gexplo

Weathering processes and crystal chemistry of Ni-bearing minerals in saprock horizons of New Caledonia ophiolite

Manuel Muñoz[a,*], Marc Ulrich[b], Michel Cathelineau[c], Olivier Mathon[d]

[a] Geosciences Montpellier, CNRS UMR 5243, Université de Montpellier, Place E. Bataillon, 34095 Montpellier, France
[b] IPGS-EOST, CNRS UMR 7516, 1 rue Blessig, 67084 Strasbourg Cedex, France
[c] Université de Lorraine, CNRS UMR 7539, CREGU, GeoRessources, 54506 Vandœuvre-lès-Nancy, France
[d] European Synchrotron Radiation Facility, 71 avenue des Martyrs, 38043 Grenoble Cedex 9, France

ARTICLE INFO

Keywords:
Nickel ore
Saprock
Boulder
New Caledonia
Kerolite
XANES

ABSTRACT

This paper proposes a detailed study of the formation of the main Ni ore that is today mined in the saprock horizon of New Caledonia ophiolite. More specifically, this study aims at, i) characterizing the nature and the crystal chemistry of the main Ni-bearing phases, and ii) better understanding the weathering processes that lead to such nickel enrichment in these horizons. The study focuses on a boulder (~20 cm in diameter) sampled in the saprock facies of the Koniambo massif, reflecting the early stages of peridotite bedrock weathering. This boulder is explored with a large panel of techniques, from the centimeter to the nanometer scale, including micro-imaging and X-ray absorption spectroscopy at the Ni and Fe *K*-edges. A characterization along the cross section reveals important heterogeneities in textures, and a large concentration of nickel in the outer part through an intense and connected Ni-phyllosilicate network that develop at the expense of the primary lizardite network. The inner part is preserved from the weathering by supergene fluids. Primary lizardite initially contains about 0.4 wt% NiO, similarly to surrounding olivine and pyroxene. In the outer part, the main Ni-bearing phases are identified as polygonal serpentine (up to ~5 wt% NiO) and two successive generations of talc-like minerals that contain ~20 to 36 wt% NiO. In these two minerals, nickel is very likely to form nano-clusters in the octahedral layers. The Fe^{3+}/Fe_{total} ratios in serpentine minerals increases regularly from ~0.5 in primary lizardite, to ~0.95 in polygonal serpentine, traducing increasing local oxygen fugacity with increasing weathering degree.

From molecular modeling, we propose that the large excess of water systematically observed for these Ni-rich minerals can be explained by nanometer sized crystals, which potentially require many additional hydrogen bonds (i.e., mainly silanol groups) to passivate crystal edges and preserve electro-neutrality. On the other hand, the main driving force leading to important nickel accumulation in the saprock horizon is likely to be the strong pH gradient present at all scales in the regolith profile, including at the boulder scale, which have major effects on the hydroxide solubility. As the pH decreases in the phyllosilicate network, we observe, i) the weathering and oxidation of the primary lizardite network, ii) the formation of a newly formed lizardite, iii) the formation of Ni-rich polygonal serpentine, iv) the formation of successive generations of Ni-rich talc-like minerals.

1. Introduction

The New Caledonia ophiolite is the world's largest outcrop of ultramafic rocks, derived from the obduction of peridotites on the continental Norfolk ridge during the Eocene at 34 Ma (Cluzel et al., 2001; Ulrich et al., 2010). It represents a world class nickel ore deposit with ~10% of the world's nickel reserves, and an annual production of > 200 kt of nickel (source USGS 2017). Because of the tropical climate, the ophiolite is strongly weathered due to the percolation of meteoric water, leading to the hydrolysis of primary minerals (olivine, pyroxene, ± serpentine), leaching of soluble elements (mainly Mg, Si) and subsequent crystallization of secondary silicate and oxyhydroxides minerals. The direct consequence of this weathering is the development of a thick and layered regolith (up to ~60 m thick) where metals of economic interests such as nickel accumulate in the different parts of the profile (Wells et al., 2009). The typical regolith in New Caledonia is composed – from the bottom to the top – of the bedrock (serpentinized peridotites), the saprock, the saprolite, the yellow limonite, the red limonite and the iron crust (including pisoliths). The accumulation of nickel ore mainly occurs in the saprock horizon, at the lower part of the

* Corresponding author.
E-mail address: manuel.munoz@umontpellier.fr (M. Muñoz).

https://doi.org/10.1016/j.gexplo.2018.12.007
Received 20 April 2018; Received in revised form 15 September 2018; Accepted 9 December 2018
Available online 13 December 2018
0375-6742/

regolith, where bulk Ni concentrations can reach up to 5 wt% (Butt and Cluzel, 2013). The regolith formation results from the combination of several phenomena that lead to the mineralogical and elemental segregation including (i) the mineral weathering/dissolution, (ii) the leaching/transport of some elements (mainly Mg and Si), (iii) the gravitational compaction of residual minerals, mainly iron oxyhydroxides (Butt and Cluzel, 2013; Pelletier, 2003; Ulrich et al., 2014). All these processes contribute to the development of a regolith that belongs to the hydrous Mg silicate type (Brand et al., 1998) where Ni mainly accumulates in the saprock horizon, in a mixture of newly formed phyllosilicate minerals.

Although the main Ni-bearing phases as well as mineral reactions that lead to Ni enrichment are still debated questions, the potential end-members for these phyllosilicate phases are: 1) the serpentine type: from Ni-lizardite to nepouite ($[Mg_xNi_{1-x}]_3Si_2O_5(OH)_4$) with $0 < x < 1$; 2) the smectite-like type: from Ni-kerolite to pimelite ($[Mg_xNi_{1-x}]_3Si_4O_{10}(OH)_2,nH_2O$) with $0 < x < 1$; 3) the talc type: from Ni-talc to willemseite ($[Mg_xNi_{1-x}]_3Si_4O_{10}(OH)_2$) with $0 < x < 1$. The crystal chemistry of these Ni-bearing phases have already been extensively characterized by different methods such as X-ray diffraction (XRD), Raman spectroscopy or Ni *K*-edge X-ray absorption spectroscopy (XAS) (e.g., Cathelineau et al., 2015; Dublet et al., 2012; Manceau and Calas, 1985; Tauler et al., 2009).

Paradoxically, the saprock horizon in the lateritic profile corresponds to the location where, 1) the first stages of bedrock weathering occur, and 2) the highest nickel concentrations are observed. Recent studies demonstrated that, in such horizon, the concentration of nickel is mainly controlled by the alkaline pH typically ranging between 8.5 and 10 due to the presence of relics of olivine (Myagkiy et al., 2017; Villanova-de-Benavent et al., 2017). However, there is currently a lack of knowledge regarding the potential relationships between weathering reactions occurring at the dissolution front of the bedrock (i.e., early weathering stages) and the nickel concentration processes in the saprock horizon. To address this question, the present work focuses on the study of a boulder rock of about 20 cm in diameter, collected on a quarry face of the open pit Cagou previously referenced as PIT-207 of the Koniambo massif (West coast of Grande Terre island; Fig. 1a, b). The outcrop presents a heterogeneous mixture composed of finely divided material (earthy material) together with decimeter-scale boulders of peridotite (Fig. 1c). The proportion of earthy material versus solid rock (i.e., boulders) evolves gradually from the bedrock to the saprolite horizon, which is typical of the saprolitic facies (Fig. 1d). In such horizon, the earthy material represents the actual nickel ore with a typical cut-off grade of about 2 wt%. The study of a boulder rock collected in the saprolitic horizon will provide crucial informations regarding the downward propagation of the weathering front in the bedrock in terms of both, the mineral reactions and the nature of fluids involved in the interaction with rocks. A large mineralogical, chemical and spectroscopic dataset will be integrated to propose models for a better understanding of both, 1) the crystal chemistry of Ni-bearing minerals, and 2) the weathering processes leading to the formation of such Ni-rich minerals in the saprock horizons of New Caledonia ophiolite.

2. Material and methods

Element mobility will first be constrained on the basis of major and trace element concentrations. In addition, micro-analysis will be performed using different techniques such as optical microscope, electron μ-probe, and μ-XRF (X-ray fluorescence) in order to characterize the distribution of minerals and elements through a cross section of the boulder. Then, the speciation of Ni and Fe will be characterized using *K*-edge μ-XANES (X-ray absorption near edge structure) spectroscopy, in order to provide information relative to the oxidation state of Fe used as a proxy of the local oxygen fugacity, potentially in relation with the presence of Ni-bearing mineral phases.

2.1. Sample preparation

A boulder of ~20 cm in diameter collected in the saprock facies of the Koniambo massif, was cut through its center with a diamond saw. The cross section was polished with variable grain sizes during 72 h so that the surface presents < 10 μm granulometric roughness (see Fig. 2). Such a preparation allows direct binocular observations and thus, to visualize the impact of the weathering on the color and texture of the rock. Moreover, the surface quality makes possible in situ chemical mapping using a laboratory μ-XRF (X-ray fluorescence) spectrometer. Four thin sections of 30 μm thickness were prepared from the mirror boulder sample along the diameter in order to perform optical microscope observations as well as Raman spectroscopy and synchrotron-based micro-analyses (see sections hereafter). In addition, each part of the boulder was isolated and powdered in order to perform bulk rock chemical analyses.

2.2. Chemical analyses

For each part of the boulder, bulk rock measurements were performed at the Service d'Analyses des Roches et des Minéraux (SARM, CRPG, Nancy, France). Major and trace element concentrations were measured respectively by ICP-OES and ICP-MS applying the analytical procedures described in Carignan et al. (2001). The full analytical procedure is available at http://helium.crpg.cnrs-nancy.fr/SARM/pages/roches.html.

In situ chemical analyses were performed by electron-probe micro-analysis (EPMA) at ISTerre (Grenoble, France), using a JEOL JXA-8230. Operating conditions were 15 kV accelerating voltage and 12 nA beam current with a 1 μm focused beam. Standardization was based on certified natural minerals and synthetic oxides: wollastonite (Si, Ca), olivine (Si, Fe, Mg), corundum (Al), orthoclase (K), rhodonite (Mn), albite (Na), and rutile (Ti). In addition, particular care was taken for the analysis of hydrated minerals, for which a clinochlore standard certified by Astimex Scientific Limited (MINM25-53 Mineral Mount) was specifically used for the analyses of Si, Fe, Mg. To ensure good reliability for such minerals, a well-crystallized and characterized antigorite crystal was systematically used as an internal standard (Merkulova et al., 2016; Muñoz et al., 2013). To further enhance the accuracy for quantitative analysis and accurate determination of the water content of minerals, ZAF correction procedure was applied using the JEOL software. The electron-probe was also used to collect element distribution maps and back-scattered electron (BSE) images.

2.3. Raman spectroscopy

Raman spectroscopy was performed at Institut Neel (Grenoble, France), using a Horiba Jobin Yvon T64000 spectrometer operating in the green light at 514.53 nm, and equipped with a 600 $g{\cdot}mm^{-1}$ grating. Raman spectra were collected using ×50 magnification objective so that the spot size was about 1 μm. The power of the laser was measured at the sample location using a photo-diode, and adjusted between 6.5 and 20 mW to avoid potential sample damage. In order to optimize the signal-to-noise ratio versus acquisition time, a typical acquisition consisted of 10 spectra accumulations collected during 30 s each. Low-, and high-wavenumber spectra were collected separately in the ranges 150–720 cm^{-1} and 3600–3750 cm^{-1}, respectively. Spectra processing including background removal and normalization was based on the Raman Processing software developed by Reisner et al. (2011). The high-wavenumber region of spectra are particularly discriminant regarding the different serpentine varieties as well as other phyllosilicates such as talc-like or smectite minerals (Auzende et al., 2004; Cathelineau et al., 2015; Rinaudo et al., 2003; Wells et al., 2009).

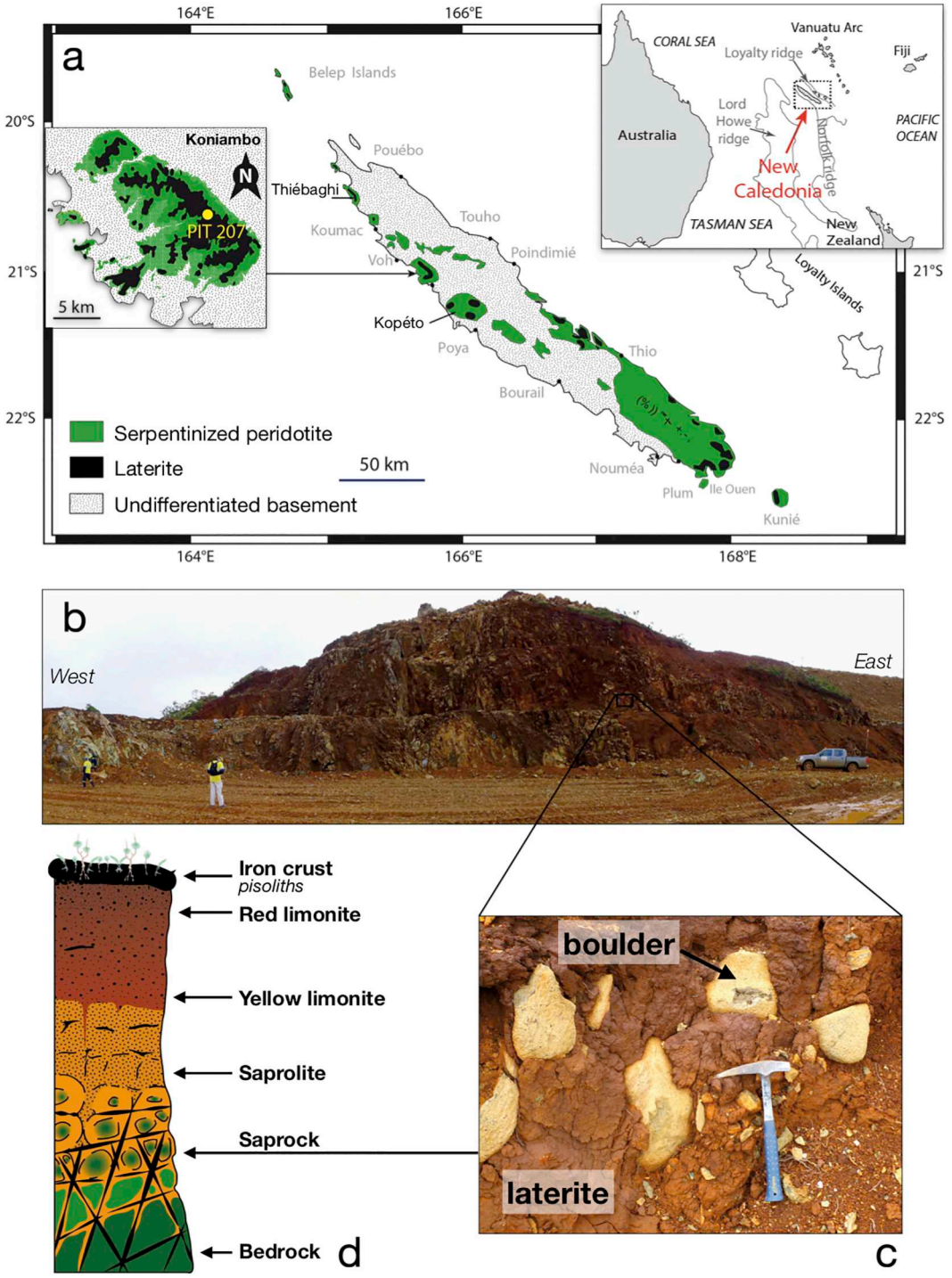

Fig. 1. a) Geological map of New Caledonia highlighting peridotite locations and the main lateritic beds; b) outcrop of the saprock facies on a query face of the Koniambo Nickel SAS mining company, c) zoom showing peridotite boulders embedded in a finely divided earthy matrix typical of the saprock facies, d) scheme of lateritic profile.

2.4. X-ray spectroscopic measurements (XRF and XANES)

Spectroscopic characterization was based on two analytical techniques: 1) micro-imaging X-ray fluorescence (μ-XRF) performed with both, a laboratory spectrometer and a dedicated synchrotron-based X-ray beam, and 2) XANES (X-ray absorption near edge structure) spectroscopy performed at the Fe and Ni *K*-edges.

2.4.1. Laboratory μ-XRF spectrometer

Large chemical maps were performed at the centimeter scale directly on the boulder slice or on thin sections using a laboratory μ-XRF, EDAX Eagle III spectrometer. A rhodium X-ray tube was operated at 20 kV and 400 μA. The X-ray beam was focused down to 40 μm in diameter thanks to the use of a polycapillary focusing optical lens. A vacuum of 10^{-6} mbar was maintained in the sample chamber to minimize the absorption of low energy X-rays by air. Fluorescence detection was achieved thanks to an EDS (energy dispersive spectrometer) with 140 eV resolution and 7 μs shaping time. Imaging acquisitions were performed with a step size of 40 μm, and a dwell time of 800 ms. Chemical maps were based on ROI (regions of interest) defined on the

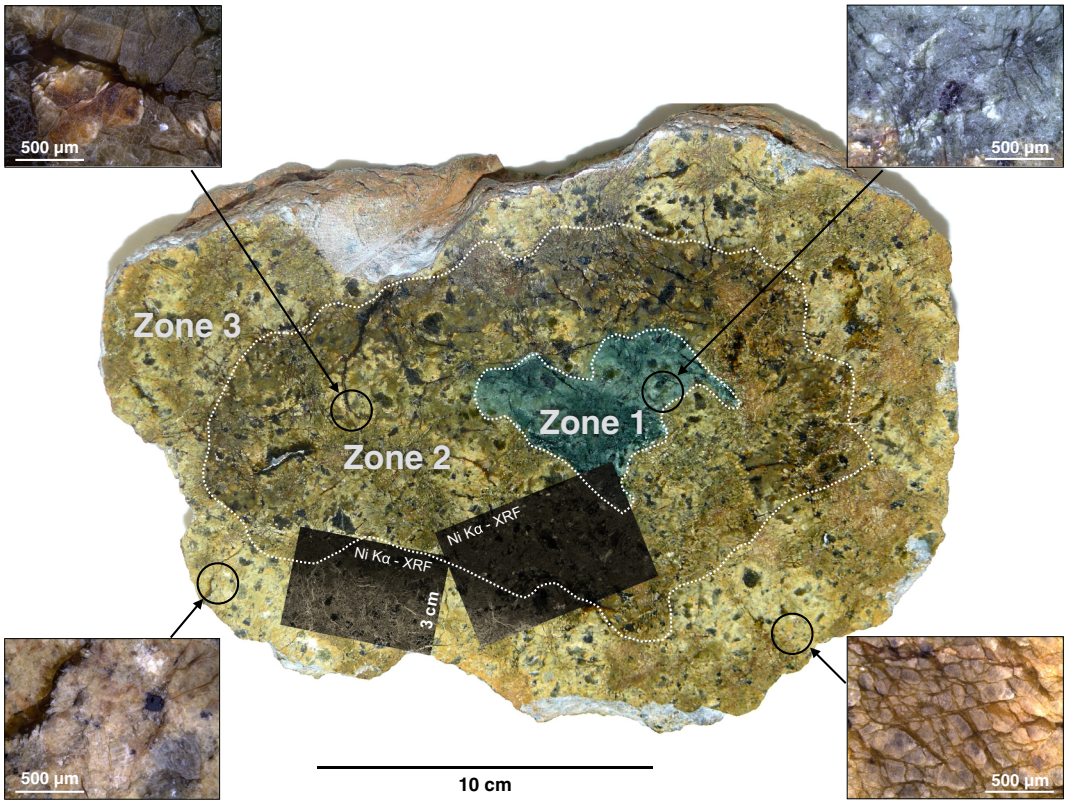

Fig. 2. Photograph of the polished cross section of the saprock boulder from the Koniambo massif of New Caledonia. Three distinct zones are observed and present different weathering levels: Zone 1 corresponds to the fresh partially serpentinized peridotite (bedrock); Zone 2 presents an intermediate weathered level; Zone 3 corresponds to a highly weathered level. Photomicrographs highlight the typical textures observed in each zone. Ni µ-XRF distribution maps are superimposed.

main *K*α lines observed on the fluorescence spectra.

2.4.2. Synchrotron measurements (XRF and XANES)

Chemical maps as well as Fe and Ni *K*-edges µ-XANES measurements were performed at the BM23 beamline of the ESRF (European Synchrotron Radiation Facility). The beamline was operating in the Multi-bunch mode, with a current of 200 mA. A fixed-exit Si(111) double-crystal monochromator was used to scan the energy around the iron and nickel *K*-edges (i.e., 7112 and 8333 eV, respectively). Harmonic rejection and X-ray beam focusing were ensured using two Pt-coated mirrors positioned at 6 mrad angle in the Kirkpatrick-Baez (KB) geometry. The size of the incident X-ray beam was 4 μm^2 in the focal plane. The sample environment consisted of using the dedicated micro-imaging experimental setup (Mathon et al., 2015). µ-XRF and µ-XANES spectra were measured in fluorescence mode using a silicon-drifted diode positioned in the horizontal plane, at 68° of the incident beam, with an energy resolution of about 140 eV. An optical microscope was used to spatially locate the position of the X-ray focal spot, and to identify specific regions on the samples.

µ-XRF maps were collected at 9.5 keV, with 5 to 10 µm sampling steps, with a dwell time of 500 ms. Chemical X-ray maps were computed using the PyMca software (Solé et al., 2007), based on pre-determined ROI of specific elements on the XRF spectra. µ-XRF elemental maps were computed based on a linear combination approach in order to convert chemical distribution information into maps of mineral phases (Muñoz et al., 2008), which makes more straightforward the interpretation of relationships between the phases (Ulrich et al., 2014). This method is based on the intensity of each fluorescence line that define a single phase, and is therefore extremely sensitive to small chemical contrasts, even when the chemical composition of minerals are relatively close to each other.

Chemical maps coupled to optical images were used to identify points of interests where µ-XANES spectra were acquired at the Fe and Ni *K*-edges. Spectra were collected with a 0.2 eV step in the pre-edge regions and 0.5 eV in the white line regions in order to extract information from both pre-edge peaks and XANES spectral signatures. Normalization was performed using the Athena software (Ravel and Newville, 2005), and pre-edge features were fitted using the XasMap package, originally dedicated to hyperspectral µ-XANES imaging (Muñoz et al., 2006). With respect to the accurate calibration protocol proposed by (Wilke et al., 2001) to quantify the $Fe(III)/Fe_{total}$ ratio, four standard samples were used to calibrate the Fe-*K* pre-edges, namely the staurolite, siderite, andradite and sanidine, prepared as pellet powders in order to prevent from any orientation/polarization effect (Muñoz et al., 2013, and references therein). Pre-edge features were fitted using three pseudo-Voigt functions with fixed shape and width, but variable position and intensity, and the tail of a Gaussian function was used to model and subtract the base-line.

Theoretical ab initio calculations were performed with the FEFF9 code (Rehr et al., 2010) in order to interpret experimental XANES features at the Ni *K*-edge. A self-consistent field (SCF card) multiple-scattering procedure was used to model charge transfer between atoms during the photo-electric process up to 4.5 Å. Full multiple scattering (FMS card) calculations were performed for the first ten shells of atoms (up to 6.0 Å) to achieve a close match between the calculated and experimental spectra and take into account the influence of the second atomic shell on spectral signatures.

3. Results

3.1. Boulder description

Fig. 2 shows a photograph of the polished cross section of the boulder. This picture reveals three main zones contrasted in color,

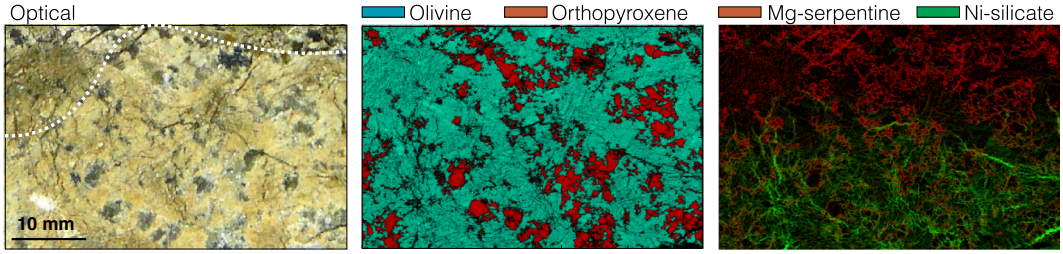

Fig. 3. (left) Optical image of an area of 30 × 46 mm in which a chemical μ-XRF map was performed. Zone 3 is located below the white dashed line and zone 2 above; (center) phase map discriminating olivine and orthopyroxene minerals. Black regions mainly correspond to silicate veins and chromite crystals; (right) phase map showing the distribution of Mg-serpentine and Ni-rich silicate veins. (For interpretation of the references to color in this figure, the reader is referred to the web version of this article.)

highlighting well different weathering levels. Each zone is separated from each other by white dashed lines. Binocular microscope images are added on the sides in order to zoom in and highlight the different textures observed in each zone (see pictures inset in Fig. 2).

Zone 1 corresponds to "fresh" green-colored peridotite. This part of the boulder presents a typical mesh texture mainly composed of olivine (Ol; green grains), few pyroxene (Px; in dark color) and a serpentine vein network formed prior supergene events. In contrast, zone 2 has a well distinct greenish to brownish color. It corresponds to an "intermediate" weathered level in the boulder. The inset zoom shows that olivine grains appear brownish, likely due to the presence of fine particles of ferric iron oxyhydroxides. The zoomed image also shows the extremity of a deeply penetrating vein coming from the external parts of the boulder to the middle of zone 2. This vein is filled with a brownish translucent material, possibly composed of a mixture of various silicates. In the external part of the boulder, i.e., the most weathered part, zone 3 displays a distinct yellowish color. Note that the earthy saprolitic matrix located all around the boulder, mainly composed of finely divided minerals such as iron oxyhydroxides as well as some silicates, was not preserved because of its powdered and non-consistent texture. The zoomed picture taken in zone 3 (left side) shows a similar penetrating vein as in zone 2, apparently filled with a similar type of brownish translucent mineral. Although olivine is still present in this zone, the mineral matrix observed all around shows smaller grain sizes with a different color, much brighter compared to olivine grains observed in zone 2. This likely indicates the presence of an intense hydrated-silicate vein network resulting from the weathering of the primary minerals, as shown in the other zoomed picture in zone 3, right side.

In order to localize areas that potentially concentrate nickel in the boulder, we collected chemical maps at the centimeter scale with a 40 μm spatial resolution, directly on the polished surface of the boulder using the laboratory μ-XRF spectrometer. Two Ni-distribution maps, based on the intensity of the Ni-*K*α emission line (7.48 keV), are superimposed to the boulder photograph (see Fig. 2), partially covering the three main concentric zones of the boulder. These two Ni-maps highlight a strong enrichment of nickel in zone 3, showing an intense network of Ni-rich veins from the outer part of the boulder up to almost the limit between zone 3 and 2 (white dashed line). In contrast, the mapped areas corresponding to zone 2 and 1 are much less intense, suggesting no significant enrichment in nickel in these zones. A much larger chemical map is presented in Supplementary material (Supp. Fig. 1) clearly showing the coronitic distribution of nickel around the boulder. However the counting statistics used for the collection of this map was not sufficient for a post-treatment. Thus, in order to highlight relationships between the different mineral phases present in zone 3, the μ-XRF map collected in the most external zone (see Fig. 2) has been processed using our linear-combination method. The results provide phase distribution maps (Fig. 3). Fig. 3 (left) shows the optical image collected in reflexion on a region of 30 × 46 mm in size, further mapped using μ-XRF. The top left part of this image, which displays a greenish color, corresponds to zone 2 in the boulder (see the white dashed line between zone 2 and 3 in Fig. 2), while the rest of the picture is more yellowish, in agreement with our previous description of zone 3. The phase map displayed in Fig. 3 (center) shows that the rock is mainly composed of olivine (Ol; turquoise color) as well as some orthopyroxene (Opx; red color) in a lesser proportion. Opx crystals appear quite homogeneously distributed relative to olivine. In this picture, black regions correspond either to silicate veins closely associated to Ol and Opx, or to chromite crystals. As detailed in Fig. 3 (right), this silicate vein network appears chemically well contrasted. The first one, in red, is identified as Mg-silicate veins, likely serpentine, and is mainly located in the internal part of zone 3, although it is still present but in a less extent in the external part (i.e., bottom part of the map). The second vein network, in green, corresponds to a Ni-bearing silicate located in the more external part of the boulder. This intense network of Ni-rich veins appears quite similar at first, but some major veins have much larger sizes, and the whole Ni-silicate network appears clearly more connected than in the Mg-serpentine network. These observations likely suggest a progressive reuse and replacement of the Mg-serpentine network by the Ni-silicate network. Moreover, such a change in texture (larger veins, and more connected) might also suggest reactions with surrounding olivine and orthopyroxene minerals.

To go into more detail in the observation scale, thin sections have been prepared corresponding to each zone of the boulder. Optical microscope images in both, polarized and crossed-polarized light are presented in Fig. 4. Zone 1 reveals a mesh-texture typical of serpentinization processes that occur in the oceanic lithosphere, possibly at mid-ocean ridge or at passive margin settings (e.g., Andreani et al., 2013; Debret et al., 2014), or during the subduction of the ophiolite (Ulrich et al., 2010). Serpentine veins intersect an olivine grain (respectively, in yellow-to-orange, and in purple-blue in crossed-polarized light; Fig. 4b) with a typical width of hundred microns or less. The serpentinization degree is estimated between 30 and 50%, in agreement with the serpentinization degree of the bedrock (Ulrich et al., 2010). Fig. 4c and d show the typical texture observed in zone 2, in which some large silicate veins penetrate deep into the boulder. These veins have larger widths of several hundredths of microns, and much lower birefringence compared to serpentine veins observed in zone 1. Such an observation suggests that the nature (mineral species, chemistry) and/or the crystallization process (grain size, porosity, etc.) is different from the serpentine network in zone 1; the latter being not preserved in zone 2. In addition, olivine grains appear significantly more divided and altered. In zone 3, the silicate-vein network is fully connected (Fig. 4e and f). Veins are merged to form large phyllosilicate domains in which crystals of olivine and pyroxene are embedded. Similarly to zone 2, phyllosilicate domains present low birefringence optical properties.

The textural evolution from the internal to the external part of the boulder highlights, 1) a complete reuse of the serpentine network in zone 2, and 2) large interconnections in the phyllosilicate network in zone 3. The low birefringence optical properties observed for the phyllosilicate minerals in zone 2 and 3 might suggest a very low

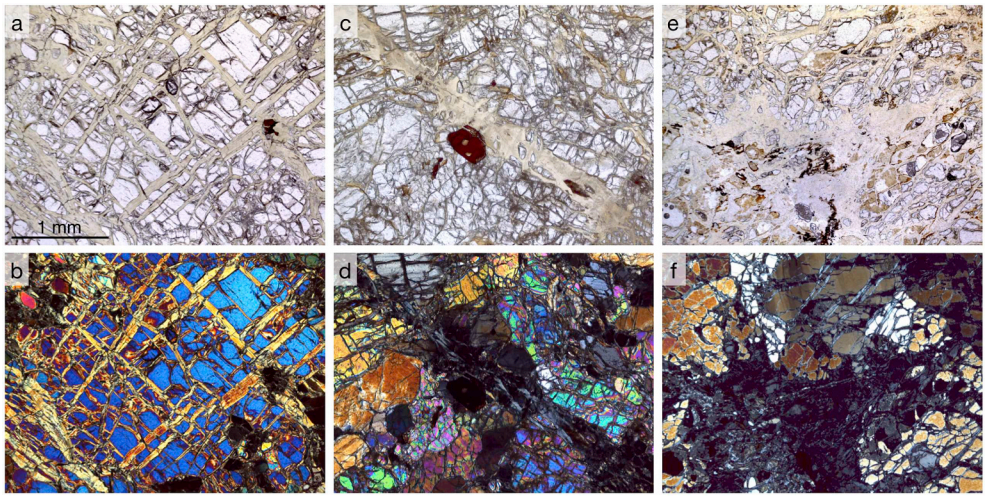

Fig. 4. Polarized (up) and crossed-polarized (down) optical images showing the typical textures observed in zone 1 (a, b), zone 2 (c, d), and zone 3 (e, f). A remarkable mesh texture is observed in zone 1, with a well-crystallized birefringent lizardite. Zone 2 highlights a deep penetration vein of amorphous phyllosilicate in weathered primary minerals, with isotropic optical properties. Zone 3 shows large amorphous phyllosilicate domains in which residues of primary minerals are embedded. (For interpretation of the references to color in this figure, the reader is referred to the web version of this article.)

crystallinity of those minerals. However, it is still difficult at this stage to accurately identify the nature of the phyllosilicate species present in the different parts of the boulder. This requires additional chemical and spectroscopic analyses (see following sections).

3.2. Mass balance and mineral chemistry

The three altered zones of the boulder have been analyzed separately in terms of both, major and trace elements by ICP-OES and ICP-MS, respectively (see Table 1). Concentrations observed in zone 1 are typical of a peridotite composition. SiO_2 content increases from zone 1 (40.22 wt%) to zone 2 (~43.40 wt%), and finally slightly decreases to 42.01 wt%. In the mean time, MgO concentration decreases from 43.58 wt% in zone 1 down to ~40.79 wt% in zone 2 and 3. The Fe_2O_3 concentration increases regularly from 7.78 wt% in zone 1 to 8.29 wt% in zone 3. On the other hand, the different zones of the boulder are highly depleted in trace elements (Table 1). Most of them are below the detection limit, except some transition metals for which the concentrations range from few ppm to hundreds of ppm (e.g., Sc, V, Co, Zn), or are above thousands of ppm (e.g., Cr or Ni). Enrichment factors of zone 3 relative to zone 1 (i.e., $100 * [C]_{zone3} / [C]_{zone1}$) highlight chemical contrast between zone 1 and zone 3. Enrichment factors for Co, Cr, V and Sc are, respectively, 5, 18, 21 and 30%. In contrast, the enrichment factor for Ni is 350%, which suggests an important external contribution for this element.

Table 1
Major and trace element bulk concentrations for the different alteration zones of the boulder. Concentrations for the following elements were below detection limit: Rb, Sr, Y, Zr, Nb, Cs, Ba, La, Ce, Pr, Nd, Sm, Eu, Gd, Tb, Dy, Ho, Er, Tm, Yb, Lu, Hf, Ta, Pb, Th, U.

	Zone 1	Zone 2	Zone 3
Oxides (wt% ± 0.01)			
SiO_2	40.22	43.40	42.01
Al_2O_3	0.59	0.60	0.63
Fe_2O_3	7.78	7.93	8.29
MnO	0.11	0.11	0.11
MgO	43.58	40.79	40.79
CaO	0.34	0.35	0.30
Na_2O	0.01	0.01	0.01
K_2O	0.01	0.01	0.01
TiO_2	–	0.02	0.02
P_2O_5	0.08	–	–
L.O.I.	5.98	5.95	6.08
Total	98.62	99.18	98.26
Elements (ppm)			
Sc	5.52	6.65	7.19
V	19.80	22.70	23.90
Cr	2442.00	2747.00	2883.00
Co	105.00	108.00	110.00
Ni	2406.00	2622.00	8418.00
Cu	–	6.63	5.55
Zn	45.00	47.20	44.80
Ga	0.49	0.56	0.60
Ge	0.70	0.84	0.86

The effect of weathering on the chemical mobility of elements can be evaluated thanks to the composition-to-volume relations proposed by Gresens (1967) and reviewed by Grant (1986, 2005). Fig. 5 presents an isocon analysis where chemical gains and losses are quantitatively evaluated by plotting the element concentrations in weathered parts of the boulder (i.e., zone 2 and 3) against those in the protolith (i.e., zone 1). Two different isocons were calculated assuming, (i) constant Al_2O_3, an element that is poorly mobile in most geological fluids, and (ii) constant volume due to little or no volume change that characterizes the bedrock to saprolite transition (e.g., Troly, 1979). Note that calculations $\Delta C^i/C_0^i$ at constant volume requires the density of rocks for the different zones of the boulder (Grant, 1986). Density measurements, performed on rock fragments using a pycnometer, were found to be 3.04, 2.99 and 2.91 for zone 1, 2 and 3, respectively. Both isocons return very similar results, which reinforces reliability in this approach. Zone 2 is mainly characterized by a significant loss of MgO and a gain of Sc and V, while other elements, including nickel, can be considered as immobile. Zone 3 is characterized by a significant loss of MgO, as well as CaO. Here again, one note a significant gain in Sc and V with a $\Delta C^i/C_0^i$ ratio of 0.25 and 0.16, respectively, at constant volume. Moreover, the external contribution of Ni (i.e., gain) in the system appears particularly important, with a $\Delta C^i/C_0^i$ ratio of 2.35. Other elements such as Al, Si, Cr, Mn, Fe, Co and Zn are mainly immobile in zone 3 (see tables in Fig. 5).

Table 2 shows the chemical composition of the main minerals observed in the three zones of the boulder. Data are given in weight percent of oxides, and are recalculated in atoms per formula unit (apfu) according to the number of oxygen atoms of each mineral specie.

To assess the accuracy of the electron probe micro-analyses, olivine and orthopyroxene grains were first measured in zone 1. In addition, an independent and well crystallized antigorite sample, previously characterized in various studies (Merkulova et al., 2016; Merkulova et al., 2017; Muñoz et al., 2013), was measured as an internal reference for the measurements of other hydrous phases. The analyses performed on Ol and Opx crystals provide structural formula that are perfectly consistent with their respective nominal compositions. The analysis of the antigorite reference sample is approximately $^{VI}[X]_{2.84}{}^{IV}[Y]_{1.97}O_5(OH)_{3.56}$, where X accounts for Mg, Fe, Mn, Ni and 1/2 Al, and Y accounts for Si and 1/2 Al, which is rather correct despite

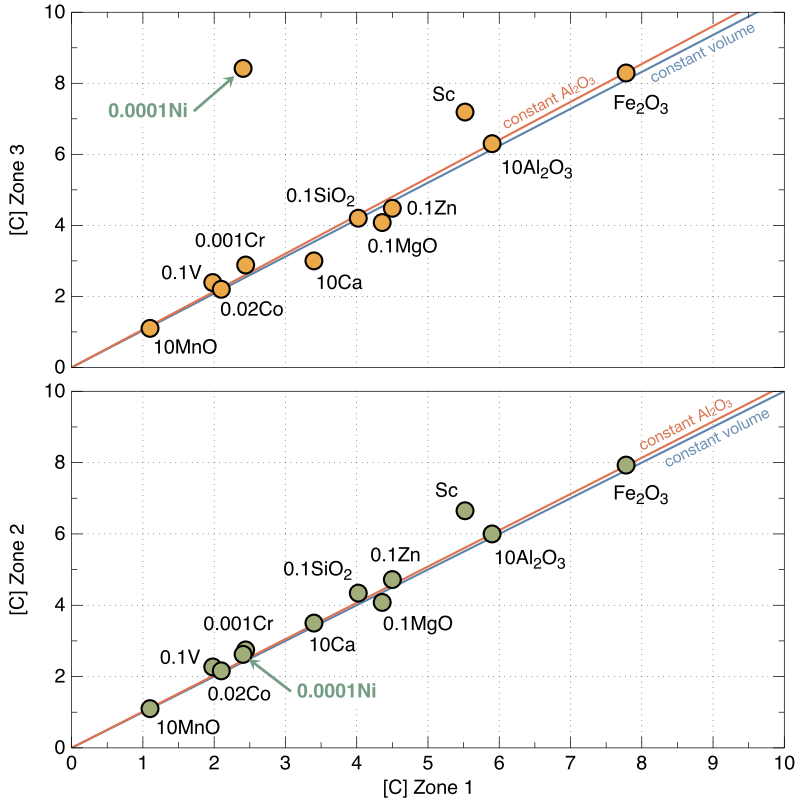

Zone 3

		ΔCⁱ/Cⁱ₀ constant Al_2O_3	ΔCⁱ/Cⁱ₀ constant volume
Loss	MgO	-0.12	-0.10
	CaO	-0.17	-0.16
Immobile	Al_2O_3	–	0.02
	SiO_2	-0.02	0.00
	Cr	0.11	0.13
	MnO	-0.06	-0.04
	Fe_2O_3	0.00	0.02
	Co	-0.02	0.00
	Zn	-0.07	-0.05
Gain	Sc	0.22	0.25
	V	0.13	0.16
	Ni	2.28	2.35

Zone 2

		ΔCⁱ/Cⁱ₀ constant Al_2O_3	ΔCⁱ/Cⁱ₀ constant volume
Loss	MgO	-0.08	-0.08
Immobile	Al_2O_3	–	0.00
	SiO_2	0.06	0.06
	CaO	0.01	0.01
	Cr	0.11	0.11
	MnO	-0.02	-0.02
	Fe_2O_3	0.00	0.00
	Co	0.01	0.01
	Ni	0.07	0.07
	Zn	0.03	0.03
Gain	Sc	0.18	0.18
	V	0.13	0.13

Fig. 5. Isocon diagrams for zone 2 and zone 3 (weathered parts of the boulder) vs. zone 1 (protolith). Oxides are plotted in wt%, trace elements in ppm. Two isocon lines are calculated on the basis of constant Al_2O_3 (in red) and constant volume (in blue), both giving similar results. (For interpretation of the references to color in this figure legend, the reader is referred to the web version of this article.)

Table 2
Chemical composition of the mineral phases observed in the different alteration zones of the boulder, expressed in percentage of weight (wt%) and in atoms per formula unit (apfu). From redox analyzes in the boulder phyllosilicates, the iron content was preferentially calculated on the basis of ferric iron oxide.

	Ref.	Zone 1			Zone 2		Zone 3				
	Atg	Ol	Opx	Lz-mesh	Lz-oliv	Lz-weath	Lz-neo	P-serp1	P-serp2	Tc-like1	Tc-like2
wt%											
Nb analysis	5	1	4	3	4	3	6	9	6	3	4
SiO_2	43.94	41.02	56.24	40.01	37.50	40.28	37.80	41.08	41.63	54.07	48.54
TiO_2	0.01	0.01	0.01	–	–	0.01	0.01	–	–	–	0.03
Al_2O_3	0.77	0.02	1.94	–	0.01	–	1.76	1.91	0.44	0.02	–
FeO	1.37	8.03	5.16	–	–	–	–	–	–	–	–
Fe_2O_3	–	–	–	5.58	9.77	6.07	7.69	4.98	6.19	0.41	0.13
MnO	0.11	0.14	0.14	0.02	0.10	0.08	0.11	0.15	0.04	0.36	0.24
MgO	41.74	50.25	34.17	41.33	39.13	37.96	36.93	31.44	33.45	17.90	8.03
CaO	0.01	0.02	0.98	–	0.03	0.04	0.04	0.10	0.08	0.02	0.04
Na_2O	–	0.01	0.01	0.01	0.01	–	0.01	0.04	0.04	0.06	0.07
Cr_2O_3	–	–	0.62	–	0.01	0.01	0.69	0.01	0.01	–	0.01
NiO	0.04	0.38	0.12	0.38	0.39	0.38	0.77	5.06	4.43	19.79	36.17
Total	87.99	99.88	99.39	87.33	86.95	84.82	85.81	84.77	86.31	92.63	93.26
H_2O	12.01	0.12	0.61	12.67	13.05	15.18	14.19	15.23	13.69	7.37	6.74
apfu											
Si	1.95	1.00	1.97	1.89	1.85	2.15	1.95	2.24	2.10	4.25	4.19
Ti	–	–	–	–	–	–	–	–	–	–	–
Al	0.04	–	0.08	–	–	–	0.11	0.12	0.03	–	–
Fe(II)	0.05	0.16	0.15	–	–	–	–	–	–	–	–
Fe(III)	–	–	–	0.20	0.36	0.24	0.30	0.20	0.24	0.02	0.01
Mn	0.01	–	0.01	–	0.01	–	0.01	0.01	–	0.03	0.02
Mg	2.76	1.83	1.79	2.91	2.88	3.02	2.85	2.56	2.52	2.10	1.03
Ca	–	–	0.04	–	–	–	–	0.01	–	–	–
Na	–	–	–	–	–	–	–	–	–	0.01	0.02
K	–	–	–	–	–	–	–	–	–	–	–
Cr	–	–	0.02	–	–	–	0.03	–	–	–	–
Ni	–	0.01	–	0.01	0.02	0.02	0.03	0.22	0.18	1.25	2.51
OH	3.56	0.02	0.15	3.99	4.30	5.40	4.89	5.54	4.62	3.87	3.94
O	5	4	6	5	5	5	5	5	5	10	10

the fact that the OH content is a little too low. The share of Al between the two sites following a Tschermak substitution is arbitrary. However, given the low Al contents in the studied minerals, the effect on structural formula calculation remains minor. Note that in the chemical description below, the reader should refer to Raman spectroscopy presented in Fig. 7, which allows the precise identification of different mineral species.

The main phyllosilicate observed within the mesh texture in zone 1 reveals a typical chemical composition of serpentine, further identified as lizardite (labelled Lz-mesh; Fig. 7) for which the structural formula is $^{VI}[X]_{3.12}{}^{IV}[Y]_{1.89}O_5(OH)_{3.99}$. In zone 2, two types of lizardite are observed. The most abundant type is labelled Lz-weath. It shows quite similar composition to that of Lz-mesh, except that the Fe content slightly increases and that the H_2O content strongly increases to 15.18 wt%. On the basis of 5 free-oxygen atoms per formula unit (i.e., not bonded to hydrogen), the resulting structural formula for this mineral is $^{VI}[X]_{3.28}{}^{IV}[Y]_{2.15}O_5(OH)_{5.40}$. The excess of OH clearly demonstrates that stoichiometric proportions of lizardite are not preserved, although the Raman spectra acquired in this zone perfectly match with the spectral signature of lizardite (Fig. 7). Therefore, such a chemical change most likely traduces an interaction between weathering fluids and primary lizardite. In addition, the fluid-mineral interaction is confirmed by a significant decrease in Mg content from 41.3 wt% in Lz-mesh, to 37.96 wt% in Lz-weath; the latter being extremely mobile in such environment (e.g., Ulrich et al., 2014). In a less extent, another type of lizardite is present in zone 2, in close association with olivine crystals (labelled Lz-oliv), and showing chemical contrasts relative to Lz-weath. The water concentration is 13.07 wt%, so that the structural formula becomes $^{VI}[X]_{3.26}{}^{IV}[Y]_{1.85}O_5(OH)_{4.30}$, in good agreement with the nominal composition of serpentine. It may be noted that the nickel concentration of the various lizardite minerals observed in zone 1 and 2 is identical and corresponds to that of olivine, 0.38 wt%. As a consequence, no nickel-enrichment is observed in these minerals between zone 1 and 2 of the boulder.

In contrast to internal parts of the boulder, the external zone (zone 3) presents three different types of serpentine minerals, labelled Lz-neo, P-serp1 and P-serp2, respectively (further described by chemical imaging and identified by Raman spectroscopy as lizardite, and polygonal serpentines, respectively). The main contrasts in terms of chemical compositions are first observed for major elements. In Lz-neo, SiO_2 concentration is lower and MgO concentration is higher than in the two other serpentine minerals. In addition, minor elements such as Al and Ni also show significant contrasts. Al_2O_3 contents are about 1.8–1.9 wt% in Lz-neo and P-serp1, while it is 0.4 wt% in P-serp2. On the other hand, NiO content is 0.8 wt% in Lz-neo, while it reaches about 5 wt% in P-serp1 and P-serp2. These differences in terms of major and minor elements make these three serpentine minerals distinct from each other. The structural formula for Lz-neo, P-serp1 and P-serp2 are, respectively, $^{VI}[X]_{3.18}{}^{IV}[Y]_{2.06}O_5(OH)_{4.89}$, $^{VI}[X]_{2.99}{}^{IV}[Y]_{2.36}O_5(OH)_{5.54}$, $^{VI}[X]_{2.94}{}^{IV}[Y]_{2.13}O_5(OH)_{4.62}$ (see Table 2). Although the structural formulae are quite far from the nominal composition of serpentine (i.e., 4 OH groups per formula unit), these three mineral species are confirmed by Raman spectroscopy (Fig. 7), and the quality of the EPMA chemical analysis is ensured by internal measurements of standard samples. Here again, the amount of hydroxyl groups is systematically and significantly higher than that of serpentine.

Finally, two other phases were identified in zone 3 in penetrative veins (described in the following section "Micro-imaging of Ni-bearing minerals") with chemical characteristics close to those of talc. However, in contrast to a pure Mg end-member of talc, the Tc-like1 shows important concentration of Ni at the expense of Mg, with up to 19.8 wt% of NiO. On the other hand, the Tc-like2 even shows a higher concentration with > 36 wt% of NiO. Raman spectroscopic analysis (Fig. 7) allows the identification of these two mineral phases, forming the Ni-silicate network previously observed in the outer part of the boulder (see Figs. 2 and 3). They both correspond to Ni-talc-like, which potentially belong to the kerolite-pimelite series according to Cathelineau et al. (2015). The structural formulae of Tc-like1 and Tc-like2 have been calculated on the basis of the structure of talc and are, respectively, $Mg_{2.10}Ni_{1.25}Si_{4.25}O_{10}(OH)_{3.87}$ and $Mg_{1.03}Ni_{2.51}Si_{4.19}O_{10}(OH)_{3.94}$. Similarly to the serpentine minerals previously described with an excess of water likely attributed to a low crystallinity degree, these Tc-like1 and Tc-like2 also present an apparent large excess of OH that reaches 3.94 in Tc-like2 (instead of 2 OH per formula unit for a pure talc composition). Moreover, the sum of divalent octahedral cations (Mg + Ni) is significantly higher than in pure talc (i.e., 3.54 instead of 3 apfu) and Si is slightly higher (4.19 instead of 4 apfu). The drifts observed in the chemical formulae of these Ni talc-like/Ni-kerolite/Mg-pimelite minerals are known since the 70's (e.g., Brindley and Maksimovic, 1974) but their origin is still subject to questioning today (Cathelineau et al., 2015). On the basis of Raman spectroscopy, the latter study demonstrates, in the case of the kerolite-pimelite series, that interstitial or interfoliar molecular water cannot explain such an excess of water, which is also in agreement with our Raman results presented hereafter.

3.3. Micro-imaging of Ni-bearing minerals

In order to understand the nature and relationships between the Ni-bearing hydrous phases in the outer part of the boulder, a large vein of about half a millimeter in width and several millimeters in length, has been characterized using various imaging techniques such as optical microscope, synchrotron-XRF, electron probe and BSE (Fig. 6). The electron probe chemical map consists of mesh of 1000 by 600 pixels, acquired with a dwell time of 200 ms and a horizontal and vertical step size of 2 µm, so that the dimensions of the map is 2 by 1.2 mm. Similarly to the µ-XRF map presented in Fig. 3, chemical information has been converted into mineral phase and displayed in three RGB (i.e., red-green-blue) maps. Fig. 6b shows the three main phases that compose the region investigated. The vein is mainly included in a large orthopyroxene crystal (in red), while only small crystals of olivine, in green, are present in the bottom-left part. The Opx crystal shows intense alteration on the edges, as well as in the cleavages and fractures (~50 µm thick). The mineral represented in blue likely corresponds to nontronite, and appears in close association with the main vein.

In Fig. 6c, the black regions of Fig. 6b are highlighted. The main phases that fill the vein are serpentine minerals (in blue). Serpentine is also observed in the fractures within orthopyroxene and olivine crystals, resulting in a large interconnected serpentine network. In the middle of the main serpentine vein, is present a smallest vein (~100 µm in width and with similar length as the serpentine vein) of Ni-rich talk-like minerals. The contact between the talk-like vein and surrounding serpentine is particularly sharp, which suggests weak chemical exchanges between these phases. Note that although contrasts are obvious in BSE and chemical imaging, no clear distinction could be made from optical microscope observations since serpentine and talc-like are both uncolored and translucent (Fig. 6a). A careful observation of the main talc-like vein (i.e., in green in Fig. 6c; labelled Tc-like2) reveals the presence of another Ni-rich talc-like phase (in red in Fig. 6c; Tc-like1). Textural relationships observed from BSE image (Fig. 6f) allow deducing a relative chronology between the two talc-like minerals: Tc-like2, which contains ~36 wt% of NiO, clearly grows at the expense of Tc-like1 that contains ~19.8 wt% NiO. The BSE image in Fig. 6e shows the extension up to the extremity of the Ni-rich vein on the right side of Fig. 6a, where the talc-like alone fills a fracture through a chromite crystal. Since no chemical exchange is expected nor observed between talc-like and chromite, such an aperture of pre-existing cracks likely results from in situ serpentinization of primary minerals, which leads to an increase in volume of about 80% (e.g., Marcaillou et al., 2011).

Fig. 6d shows the distribution of the different types of serpentine minerals observed in zone 3 (i.e., Lz-neo, P-serp1 and P-serp2), and

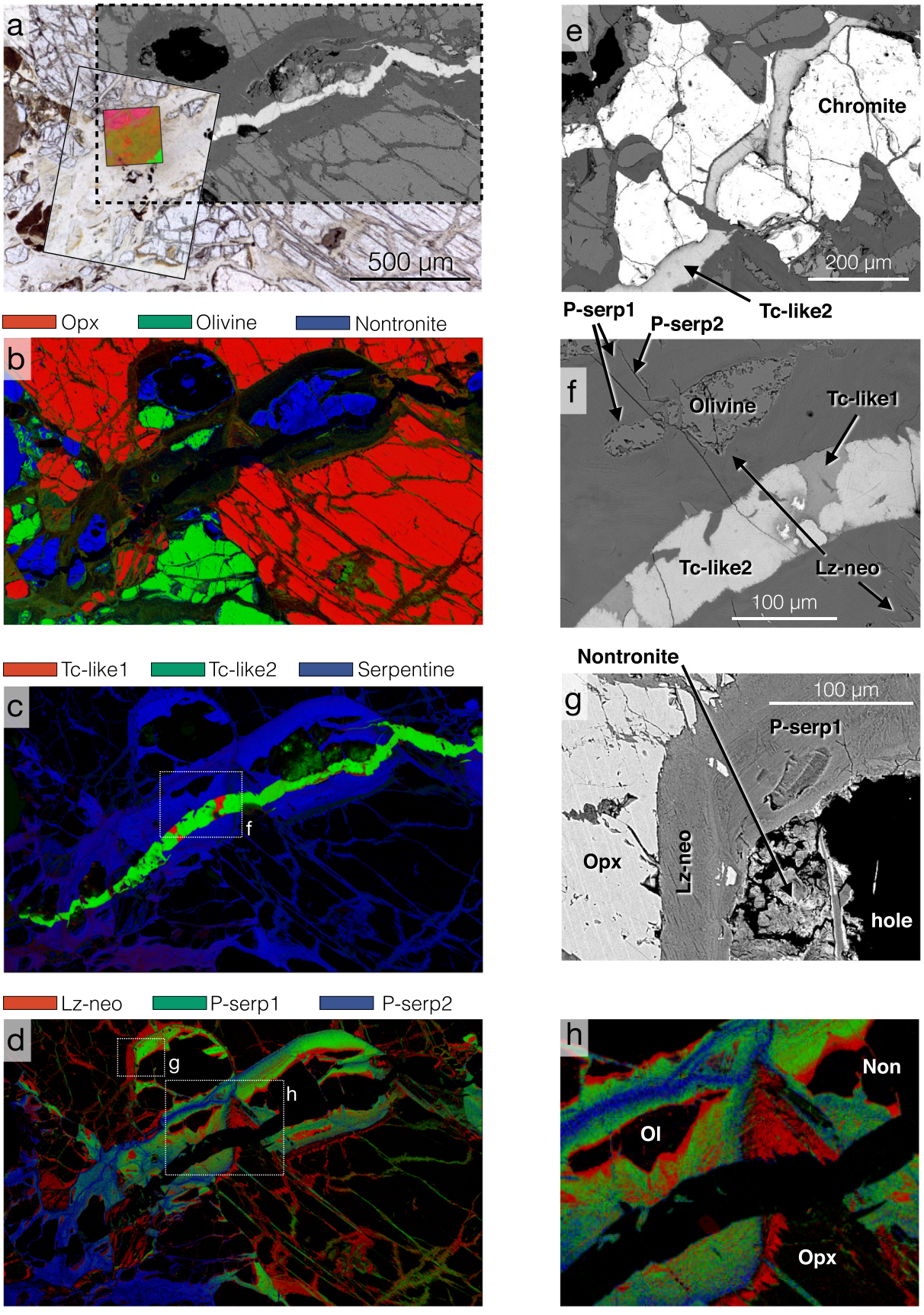

(caption on next page)

Fig. 6. Micro-imaging of a Ni-rich vein typical of zone 3. a) Optical image corresponding to the area that has been chemically mapped using electron micro-probe; including three superimposed images, from the largest to the smallest: (i) BSE image, (ii) optical before electron probe chemical maps, (iii) synchrotron μ-XRF map showing Fe and Ni distribution, respectively in red and green. b), c) and d) Phase maps in RGB (red-green-blue) calculated from electron-probe chemical imaging showing the distribution of orthopyroxene, olivine, nontronite, two types of Ni-rich talc-like (Tc-like1 and Tc-like2), and three types of serpentine (Lz-neo, P-serp1 and P-serp2). e), f) and g) BSE images highlighting micro-textures and relationships between the different phases observed. h) Zoom in d) showing the relationships between different types of serpentine and the surrounding minerals. (For interpretation of the references to color in this figure legend, the reader is referred to the web version of this article.)

highlighted by phase map calculations thanks to small chemical contrasts (Table 2). Lz-neo (in red) clearly appears in close association with primary minerals. It develops in cleavage planes and fractures, but also fully surrounds the Opx with a fringe of about 50 μm thick (see also BSE image; Fig. 6g). The fact that Lz-neo, 1) is observed on the walls of the main thick vein (i.e., > 500 μm), and 2) contains about twice the amount of nickel compared to lizardite observed in zone 1 and 2, demonstrates that it is not inherited from previous serpentinization events but is rather developed in situ during supergene weathering. In addition, this Lz-neo is also observed around the olivine (Ol) and nontronite (Non) crystals (see zoom presented in Fig. 6h) and therefore likely develop at their expense. Although most of the contact surface is quite sharp between Lz-neo and P-serp1-2, the extremity of the former Opx crystal (in red; Fig. 6h), cross-cut by the Ni-talc-like vein, shows a quite diffuse contact and then suggests chemical exchanges. Moreover, the width of Lz-neo fringe remains roughly constant at ~50 μm, whereas the main serpentine vein has a thickness that increased up to ~500 μm, in strong contrast with the vein sizes observed in zone 1. Such an observation also reinforces the fact that P-serp1 and P-serp2 crystallization results from the interaction between Lz-neo and a Ni-bearing supergene fluid.

Finally, P-serp1 and P-serp2, both containing about the same amount of NiO, between 4.5 and 5 wt%, appear relatively mixed with each other in the central part of the mapped area (Fig. 6d and zoom in Fig. 6h). However, the P-serp1 (in green), for which the concentration in aluminum is significantly higher than in P-serp2, appears rather associated to the orthopyroxene in the right side of the mapped area. On the other hand, P-serp2 (in blue), less concentrated in Al, is rather associated to olivine crystals located in the bottom-left part of the mapped area. This also suggests a link between primary minerals and Ni-rich polygonal serpentine. Considering the fact that olivine is more abundant, P-serp2 is likely to be the most representative serpentine composition in zone 3.

3.4. Raman characterization of main phyllosilicate minerals

Fig. 7 presents a compilation of the most representative Raman spectra collected on the mineral species described above. Spectra were collected in low and high wavenumber ranges in order to characterize, respectively, the structural atomic bonds and the hydroxyl bonds. The main phyllosilicate observed in zone 1 presents unambiguously the spectral signature of lizardite (e.g., Auzende et al., 2004), most likely inherited from previous tectonic regime. Lz-weath observed in zone 2, almost presents the same spectral characteristics as Lz-mesh. However, one can observe a slight shift of the band at 687 cm^{-1} towards higher wavenumbers, and a rapprochement of the OH bands at 3685 and 3703 cm^{-1}. This is consistent with the change in terms of optical properties of serpentine minerals between zone 1 and 2 as described in Fig. 4, traducing a weathering and possible change in crystallinity of the former lizardite. In zone 3, various phyllosilicate species are observed, as described in Fig. 6. Lz-neo presents spectral features that are consistent with those of lizardite, with the same small differences as observed for Lz-weath (i.e., peak shifts observed at 687, 3685 and 3703 cm^{-1}). For P-serp1 and P-serp2, however, if the low wavenumber domain is pretty similar to the spectral signature of lizardite, the high wavenumber region shows major differences: the two main vibration bands located at 3685 and 3703 cm^{-1} in Lz-mesh, shift at 3689 and 3698 cm^{-1}, respectively, and their relative intensities are inverted. These changes are perfectly consistent with the occurrence of polygonal serpentine (e.g., Auzende et al., 2004). Finally, distinct spectral features are observed for Tc-like1 and Tc-like2. In the 100–700 cm^{-1} domain, the main vibration bands are perfectly consistent with those of talc. However, in the OH region, one can observe three different bands located at 3627, 3648, 3665 cm^{-1}. According to Cathelineau et al. (2015), these three peaks correspond to those of talc-like minerals showing a substitution rate of Mg by Ni of about 71 at.%. Note that this is in perfect agreement with the structural formula calculated for Tc-like2 (see previous section "Mass balance and mineral chemistry") that

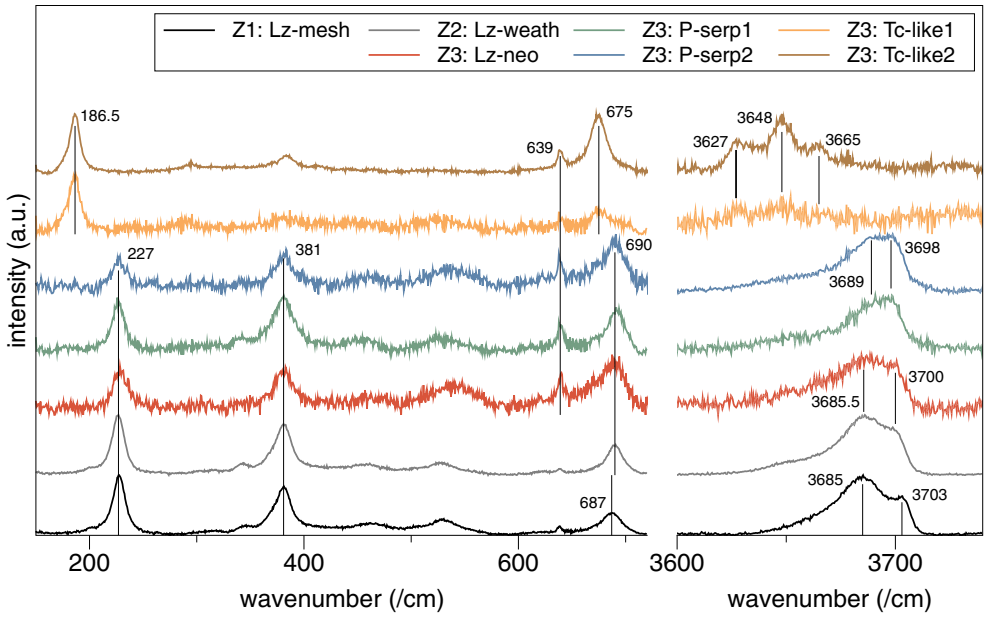

Fig. 7. Raman spectra collected for the different types of phyllosilicate minerals observed in different parts of the boulder. Zone 1 and 2 mainly contain lizardite, Lz-mesh and Lz-weath, respectively. Zone 3 presents a neo-formed lizardite (Lz-neo) as well as two chemically distinct polygonal serpentine (P-serp1 and P-serp2), and talc-like minerals (Tc-like1 and Tc-like2). Spectral features are presented at low and high wavenumber in order to highlight, respectively, main structural atomic bonds and hydroxyl bonds.

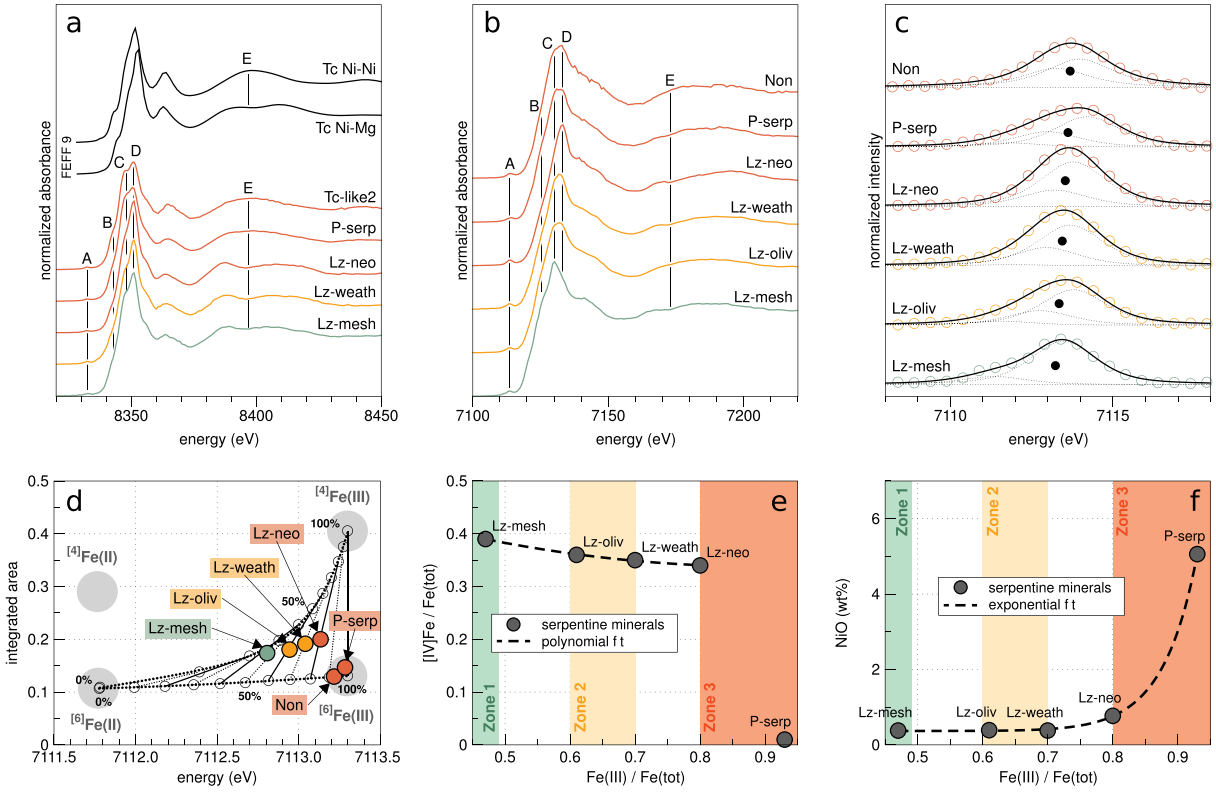

Fig. 8. Analysis of the speciation of nickel and iron in the main phyllosilicate minerals observed in zone 1, 2 and 3 (respectively, in green, orange and red). a) Normalized XANES spectra collected at the Ni *K*-edge, and ab initio theoretical calculations (FEFF 9; black solid lines) performed from the typical structure of talc showing the main influence of the second neighbors of nickel (i.e., Ni-Mg and Ni-Ni; feature E). b) Normalized XANES spectra collected at the Fe *K*-edges. c) Background subtracted Fe-*K* pre-edge features showing: experimental data (empty circles), peak deconvolution (dashed lines), pre-edge fit (black solid lines), pre-edge centroid (black circles). d) Pre-edge centroids plotted in a variogram showing the amount of the different Fe species (i.e., oxidation state and coordination number). e) Relation between tetrahedral iron and ferric iron relative to total iron in serpentine minerals. f) Exponential correlation between the concentration of Ni and the oxidation state of Fe in serpentine minerals. (For interpretation of the references to color in this figure legend, the reader is referred to the web version of this article.)

proposes a Mg/Ni substitution rate of 70.90 at.%. Moreover, a general observation is that for each spectrum presented in Fig. 7, no H_2O molecule was detected in the high wavenumber region, but only hydroxyl groups.

3.5. Nickel speciation and iron redox

To further characterize the crystal chemistry of mineral phases that result from weathering processes, synchrotron µ-XANES analysis have been performed at the Ni and Fe *K*-edges. Fig. 8a shows µ-XANES spectra collected at the Ni *K*-edge for the Ni-bearing phyllosilicate minerals observed in the different zones of the boulder. In contrast to iron, nickel remains divalent in most natural environments, and is only present in octahedral sites in phyllosilicate minerals as well as in most silicate and oxide minerals (e.g., Farges et al., 2001a; Manceau and Calas, 1986). Therefore, the pre-edge peak (feature A), known to be mainly sensitive to the coordination environment (e.g., Farges et al., 2001b; Muñoz et al., 2005) remains almost constant in our data set. The feature B located in the edge of the spectra does not show any significant change. In contrast, the double peak located in the white line presents a progressive increase of the feature D relative to C from Lz-mesh to Lz-neo. In P-serp and Tc-like2, the intensity of feature D is significantly lower than in lizardite minerals. Interestingly, the first EXAFS oscillation, located between 8380 and 8430 eV shows a clear contrast between the three lizardite minerals on one hand, and P-serp and Tc-like2 on the other hand (see feature E).

To further understand such a difference in the spectral signatures (i.e., feature E), ab initio XANES calculations, extended up to 8450 eV, have been performed based on the structure of talc (Perdikatsis and Burzlaff, 1981). The result corresponds to the spectrum labelled "Tc Ni-Mg" in Fig. 8a, which clearly shows the typical hollow in the first EXAFS oscillation (feature E), as observed for lizardite minerals. Another calculation has been performed on a modified structure of talc, in which the first Mg (Z = 12) neighbors (i.e., 6 Mg located at 3.05 Å) have been replaced by Ni (Z = 28) neighbors. The contrast in atomic number between Mg and Ni is sufficient (> 10) to expect significant changes in the spectral response based on such cationic substitution (Teo, 1986). The result corresponds to the spectrum labelled "Tc Ni-Ni" in Fig. 8a. The feature E highlights a clear and significant difference according to the type of second neighbors around the photo absorber atom. In case Mg is present in the 2nd neighbor atomic-shell, a hollow is observed in the EXAFS oscillation, whatever the type of phyllosilicate observed (Muñoz et al., 2013). In contrast, if nickel is present in the 2nd atomic shell, the oscillation appears more regular and no hollow is observed. As a result, such a difference observed in the EXAFS oscillation (feature E) does not directly reflect the nature of minerals, but rather the atomic number of the second-neighbor atoms, and therefore the nature of second atomic shell beyond the first shell of oxygen (i.e., short distance structural information; < 1 nm). In other words, XANES spectroscopy here allows to assert – in the case of P-serp and Tc-like2, containing around 5 and 36 wt% NiO, respectively – that octahedral nickel (i.e., $^{[VI]}$Ni) mainly forms bonds with nickel as second neighbor: $^{[VI]}$Ni—O—$^{[VI]}$Ni, while a minor/negligible part only may form bonds with magnesium second neighbors: $^{[VI]}$Ni—O—$^{[VI]}$Mg. Consequently, such an oscillation observed for these two minerals likely traduces the fact that nickel is not homogeneously distributed within the structure,

but most likely forms Ni-clusters in the octahedral layers. This conclusion, simply based here on XANES spectra analysis, is consistent with EXAFS analyses performed on both, the 7 Å and 10 Å phyllosilicate phases observed in New Caledonia laterites (Dublet et al., 2012; Manceau and Calas, 1985). Nickel is likely to form nano-clusters in the octahedral layers of either serpentine-like or talc-like Ni-bearing minerals in lateritic horizons.

Fig. 8b presents XANES spectra collected at the Fe *K*-edge for the main phyllosilicate minerals observed in the different zones of the boulder. From Lz-mesh to Lz-neo, the white line region of the spectra shows quite regular changes. Feature B decreases in intensity, while the intensities of features C and D are progressively inverted. The white lines for polygonal serpentine (P-serp) and nontronite (Non) present a relatively intermediate signature, and only a small contrast is observed in the first EXAFS oscillation (i.e., feature E), which does not have a hollow like in the other cases. The oxidation state of iron has been determined thanks to the analysis of the pre-edge peaks (feature A). Fig. 8c shows the background subtracted pre-edge peaks that have been deconvoluted thanks to three pseudo-Voigt functions. The centroid was calculated for each pre-edge peak based on a deconvolution fitting procedure. Then, centroid energy and intensity were, respectively, interpreted in terms of Fe^{3+}/Fe_{total} ratio and percentage of octahedral and tetrahedral iron thanks to the use of appropriate model compounds and calibration (see Material and methods section, and references therein). The pre-edge centroid positions are reported in a variogram showing the amount of the different Fe species, i.e., average oxidation states and coordination numbers (Fig. 8d). Fit parameters and results are listed in Table 3. Centroid energy values increase continuously from the inner part to the outer part of the boulder, which is traduced by an increase of the Fe^{3+}/Fe_{total} ratio from 0.47 in Lz-mesh up to 0.80 and 0.93 for Lz-neo and P-serp, respectively, in zone 3. Nontronite shows a Fe^{3+}/Fe_{total} ratio of 0.99, which is consistent with its nominal formula. These results indicate that, 1) the weathering of the bedrock occurs under highly oxidizing conditions, and 2) iron in serpentine minerals is an excellent proxy to determine the exposure level to external fluids, and thus the weathering level of the rocks.

On the other hand, as suggested by Wilke et al. (2001), the average coordination number of iron can be directly deduced from the integrated area of the pre-edge peaks reported in the speciation variogram of iron (Fig. 8d). In this variogram, the evolution of the integrated area from ferrous to ferric iron in a six-fold coordinated environment, i.e., octahedral site in the case of phyllosilicate minerals (Muñoz et al., 2013), is almost linear. In contrast, such an evolution for four-fold coordinated environment, i.e., tetrahedral sites, is strongly non-linear. This makes the "vertical" reading of the variogram relatively difficult, and induces a large uncertainty on the determination of the average coordination number of iron. Nevertheless, Table 3 summarizes the estimations of the $^{[IV]}Fe/Fe_{total}$ ratio, including uncertainties related to the reading of the oblique lines plotted in the variogram, and connecting iso ferric-to-ferrous contents with different coordination numbers. However, the uncertainties also depend on the determination of Fe^{3+}/Fe_{total} ratio and therefore can potentially be more important. Once that is considered, and despite the fact that the centroid intensity increases continuously in lizardite minerals from zone 1 to 3, the estimations for the occurrence of tetrahedral iron are, respectively, 39, 36, 35 and 34% of total iron for Lz-mesh, Lz-oliv, Lz-weath and Lz-neo. Unexpectedly, the relative amount of tetrahedral iron in the structure of lizardite is therefore inversely correlated to the relative amount of ferric iron (Fig. 8e). This, however, certainly requires a more robust quantitative analysis using Fe *K*-edge EXAFS spectroscopy in order to assess the reliability of pre-edge information regarding the quantitative determination of the average coordination number. Even so, the transition to polygonal serpentine (P-serp) is marked by a strong change in the average coordination number. Indeed, the $^{[IV]}Fe/Fe_{total}$ ratio decreases drastically to about 0.01, suggesting that only octahedral (and mainly ferric) iron is present in the structure of polygonal serpentine. Similarly, the centroid value of nontronite indicates a $^{[IV]}Fe/Fe_{total}$ ratio of about 0.06 for a Fe^{3+}/Fe_{total} ratio of 0.99, which is in excellent agreement with its structural formula that can be approximated as $Fe_2Si_4O_{10}(OH)_2,n(H_2O)$.

Fig. 8f shows a correlation diagram of the nickel concentration in serpentine minerals observed in zone 1, 2 and 3 of the boulder, as a function of the Fe^{3+}/Fe_{total} ratio. The nickel content remains constant at about 0.4 wt% in the intermediate weathering level of zone 2, as it is in zone 1. This suggests that external Ni-rich fluids do not reach directly the inner part of the boulder. However, pervasive penetration of water is likely to occur since, 1) the average oxidation state of Fe increases significantly, and 2) the mesh lizardite of zone 1 is no longer observed, and the main lizardite in zone 2 appears weathered and shows an excess of water (see Fig. 4 and Table 2). In zone 3, nickel content increases significantly in the neoformed lizardite as well as in polygonal serpentine while the oxidation state of iron is still increasing. It comes that the nickel content rises exponentially with the oxidation of iron in serpentine minerals.

4. Discussion

4.1. Structure and chemistry of Ni-bearing minerals

4.1.1. Prerequisites of literature for the discussion on crystal chemistry

The crystal chemistry of Ni-bearing phyllosilicate minerals present in ultramafic saprolite horizons of New Caledonia have been extensively studied using different chemical and structural characterization techniques (e.g., Cathelineau et al., 2015; Dublet et al., 2012; Manceau and Calas, 1985; Wells et al., 2009). It is commonly admitted that these minerals mainly belong to different Mg-Ni solid-solutions involving 1:1 phases, i.e., the lizardite-nepouite series $[Mg_xNi_{1-x}]_3Si_2O_5(OH)_4$ with $0 < x < 1$, and 2:1 phases such as the talc-willemseite $[Mg_xNi_{1-x}]_3Si_4O_{10}(OH)_2$ with $0 < x < 1$, and kerolite-pimelite $[Mg_xNi_{1-x}]_3Si_4O_{10}(OH)_2,nH_2O$ with $0 < x < 1$ series, also called the talc-like series (Pelletier, 1996). The typical limit used to distinguish Ni-kerolite from pimelite is a Ni content of 1.5 apfu (Wells et al., 2009). For high nickel contents, Manceau and Calas (1985) demonstrate that nickel forms nano clusters within the octahedral layers either in the 1:1 or 2:1 phases. They propose that Ni domains extend in the range 20–60 Å in serpentine type minerals, and 15–40 Å in the 2:1 phases. From spectroscopic characterizations, the same authors suggest a relatively low crystallinity for these minerals, with coherent domains of 20–30 nm at maximum. Moreover, HR-TEM image of a Ni-kerolite nano-crystal shows a size of about 30 nm in *c* direction, while the extent

Table 3
Fit parameters of Fe-*K* pre-edge peaks, and corresponding Fe^{3+}/Fe_{total} and $^{[IV]}Fe/Fe_{total}$ ratios.

Zone in boulder	Mineral type	Centroid energy (eV)	Centroid intensity	Fe^{3+}/Fe_{total}	$^{[IV]}Fe/Fe_{total}$
1	Lz-mesh	7112.81 (0.05)	0.173 (0.005)	0.47 (0.10)	0.39 (0.10)
2	Lz-oliv	7112.94 (0.05)	0.180 (0.005)	0.61 (0.08)	0.36 (0.09)
2	Lz-weath	7113.04 (0.05)	0.192 (0.005)	0.70 (0.07)	0.35 (0.08)
3	Lz-neo	7113.13 (0.05)	0.200 (0.005)	0.80 (0.05)	0.34 (0.07)
3	P-serp	7113.22 (0.05)	0.129 (0.005)	0.93 (0.05)	0.01 (0.06)
3	Non	7113.28 (0.05)	0.146 (0.005)	0.99 (0.04)	0.06 (0.05)

in the *ab* plane is rather about 100 nm (Cathelineau et al., 2015).

Despite numerous chemical and structural studies, most of these phases remain enigmatic, as discussed by Cathelineau et al. (2016). On a chemical basis for example, these authors show that Si/(Si + Mg + Ni) ratios for kerolite do not match with that of talc or serpentine, and different hypotheses were proposed such as the mixing of talc with additional brucite layers (Brindley and Hang, 1972), or with additional serpentine layers (Villanova-de-Benavent et al., 2014). However, these assumptions could not be confirmed by HR-TEM direct observations (Cathelineau et al., 2015; Cathelineau et al., 2016). In addition, electron-microprobe analyses never get 100%, meaning that large amounts of interfoliar molecular water should be considered, in agreement with the typical formula of kerolite and pimelite. But here again, molecular water in such minerals has not been demonstrated so far by Raman spectroscopy (Cathelineau et al., 2015).

Finally, XRD study performed on Ni-kerolite shows a typical *d*(001) spacing at about 9.6 Å (Brindley et al., 1979; Wells et al., 2009), which is significantly higher than 9.35 Å typically observed for talc. The latter authors attributed such an increase of the basal spacing to randomly stacked layers. It is worth noting that the hydrothermal synthesis of talc and Ni-bearing talc leads to the formation of nano-particles with a crystallinity degree that is proportional to time-duration of the synthesis, and inversely proportional to the temperature (Dumas et al., 2013; Dumas et al., 2015). The typical crystal size obtained after a few hours (< 10 h) and ~300 °C is about 100 nm in the *ab* plane and 200 nm in the *c* direction, with a *d*(001) basal distance of ~9.5 Å. At lower temperature, i.e., 100 °C, crystal sizes are smaller and the basal distance can increase up to ~10 Å (Dumas et al., 2015). Based on these studies, one can infer that low crystallization temperature could explain such a low particle sizes observed, for example, for the kerolite-pimelite minerals in saprock horizons.

4.1.2. Crystallochemistry model of nickel-rich hydrated silicates

The detailed mineral study of the boulder characteristic from saprock horizons in New Caledonia ophiolite reveals the presence of various Ni-bearing minerals. These minerals are mainly located in the most external part and appear as an intense and connected network. Based on Fe *K*-edge XANES spectroscopy, we demonstrate that the oxidation state of iron in serpentine minerals increases progressively with Fe^{3+}/Fe_{total} ratios from about 0.45 in the internal/non-weathered part, to ~0.95 in the external/highly-weathered part. We also demonstrate that the most oxidized serpentine minerals correspond to the higher Ni concentrations (about 5 wt% NiO) with a positive exponential correlation (Fig. 8f). In addition, the latest stage of mineralization likely corresponds to the more Ni-enriched phases identified as talc-like. The first one (Tc-like1) contains about 20 wt% of NiO while, the latest one (Tc-like2), crystallizing at the expense of the first one, contains > 36 wt %. In addition, Ni *K*-edge XANES results show that Ni likely forms nano-clusters within octahedral layer, either in Ni-rich polygonal serpentine or talc-like minerals, as it was already demonstrated by Ni *K*-edge EXAFS spectroscopy for such minerals (Dublet et al., 2012; Manceau and Calas, 1985). It is worth noting that each of these Ni-rich phases shows a strong excess of the hydroxyl content: up to 5.5 apfu – instead of 4 – for the polygonal serpentine, and up to 3.94 apfu – instead of 2 – for talc-like (see Table 2).

In order to understand the OH excess typically observed for kerolite, we propose a "molecular" model of talc. The structure used is that refined by Perdikatsis and Burzlaff (1981). This model was restricted in size to about 20 Å in both the *ab* plane and the *c* direction (see Fig. 9). It initially accounts for 134 Mg (orange atoms), 186 Si (grey atoms), 106 OH (yellow atoms), 536 O (only represented in full size in transparent blue). However to better illustrate the nickel concentration and speciation, 95 Mg atoms were replaced by Ni (green atoms), in agreement with the Mg-to-Ni substitution rate observed in Tc-like2. On the basis of 10 oxygen atoms, the resulting structural formula is $Mg_{0.73}Ni_{1.77}Si_{3.47}O_{10}(OH)_{1.98}$. This strongly contrasts from the structural formula calculated for Tc-like2, $Mg_{1.03}Ni_{2.51}Si_{4.19}O_{10}(OH)_{3.94}$, where all the coefficients are significantly higher, and the amount of OH is doubled. However at this stage, this molecular model suffers from electro-neutrality since many oxygen atoms located at the edge in the *ab* plane lost part of their bonds to cationic neighbors. To correct this, the edges of the "molecular" crystal were passivated by adding hydrogens (in red; Fig. 9). Apart a few hydrogens required in the octahedral layers to form new hydroxyl groups (only 16 in total), most of the hydrogen bond to free oxygens in the tetrahedral layer to form silanol groups; in agreement with a recent experimental study (Blanchard et al., 2018). In total, 106 hydrogens were required to passivate the whole crystal structure so that the amount of hydrogen is twice the initial amount (i.e., 106 hydroxyl groups initially present). Based on these new proportions, the structural formula becomes $Mg_{0.91}Ni_{2.21}Si_{4.33}O_{10}(OH)_{4.93}$, which matches relatively good with that of Tc-like2. However, the fact that Mg and Si are slightly lower and OH slightly higher probably means that the real particle size must be larger in the *ab* plane. Indeed, expanding the model in the *c* direction does not affect stoichiometric proportions, while an expansion in the *ab* plane will result in a faster increase of Mg, Ni and Si relative to OH.

It should be noted that this model is not intended to explain the actual structure of kerolites/talc-like, and other structural models cannot be excluded (i.e., mineral mixtures, crystalline defects, porosity, etc.). However it demonstrates the major effect of the proton passivation of nano-crystals on the high hydroxyl contents generally observed by microprobe analysis, and the lack of molecular water highlighted by Raman spectroscopy (Cathelineau et al., 2015; present study). The nanometer crystal size also makes possible to explain the almost isotropic optical properties highlighted from crossed-polarized microscope observations. It is likely that similar reasoning may not only be applied to our talc-like minerals (zone3), but also to polygonal serpentine (zone 3) and weathered lizardite (zone 2).

Lastly, the question of structural differences observed in the *d*(001) basal distance remains (Brindley et al., 1979; Wells et al., 2009). To provide some answers, we performed a structural relaxation of the added hydrogens only (in red; Fig. 9) using the molecular dynamics module of the CrystalMaker® version 9.2.9 software. After stabilization of Monte Carlo iterations (about 400,000 in total) the structural model shows that silanol groups located at the bottom and the top of the two-layered molecular model are oriented through the external part of the nano-crystal. In addition, the silanol groups located within the interfoliar space clearly point at the opposite from each other, suggesting a significant proton-proton repulsion. Such a force opposes to van der Waals force, which may result in an increased interfoliar distance. Moreover, the ionic radius of nickel in octahedral environment is slightly smaller than that of magnesium, i.e., 0.69 Å and 0.72 Å, respectively (Shannon, 1976). Therefore, a large substitution rate will also result in the contraction of the TOT layer, and a further increase of the interfoliar distance. It is thus probable that the reduction of the particle sizes in the *ab* plane, potentially coupled with a high Mg-Ni substitution rate, makes it possible to obtain *d*(001) basal distances such as those observed for talc-like particles. As an attempt, and despite the fact that proper molecular dynamics requires in-depth work and strong control of interatomic potentials and the boundary conditions of the models, the full relaxation of the molecule presented in Fig. 9 has been performed. Results are shown in Supplementary material (Supp. Fig. 2). Interestingly, after the almost complete relaxation (Supp. Fig. 2b), silanol groups show similar positions than in Fig. 9 (also shown in Supp. Fig. 2a). However, significant contraction of the TOT layer due to the reduction of Ni−O distances is observed, together with the distortion of octahedrons. In addition, proton-proton repulsion forces lead to an increase of the interfoliar distance, and finally an increase of the *d*(001) basal distance. Such results perfectly comfort our crystallochemical model previously described.

As a conclusion, the enigmatic crystal chemistry of the kerolite-to-pimelite series typically observed in the saprolite horizon of New Caledonia ophiolite, could be, at least partially, solved thanks to our

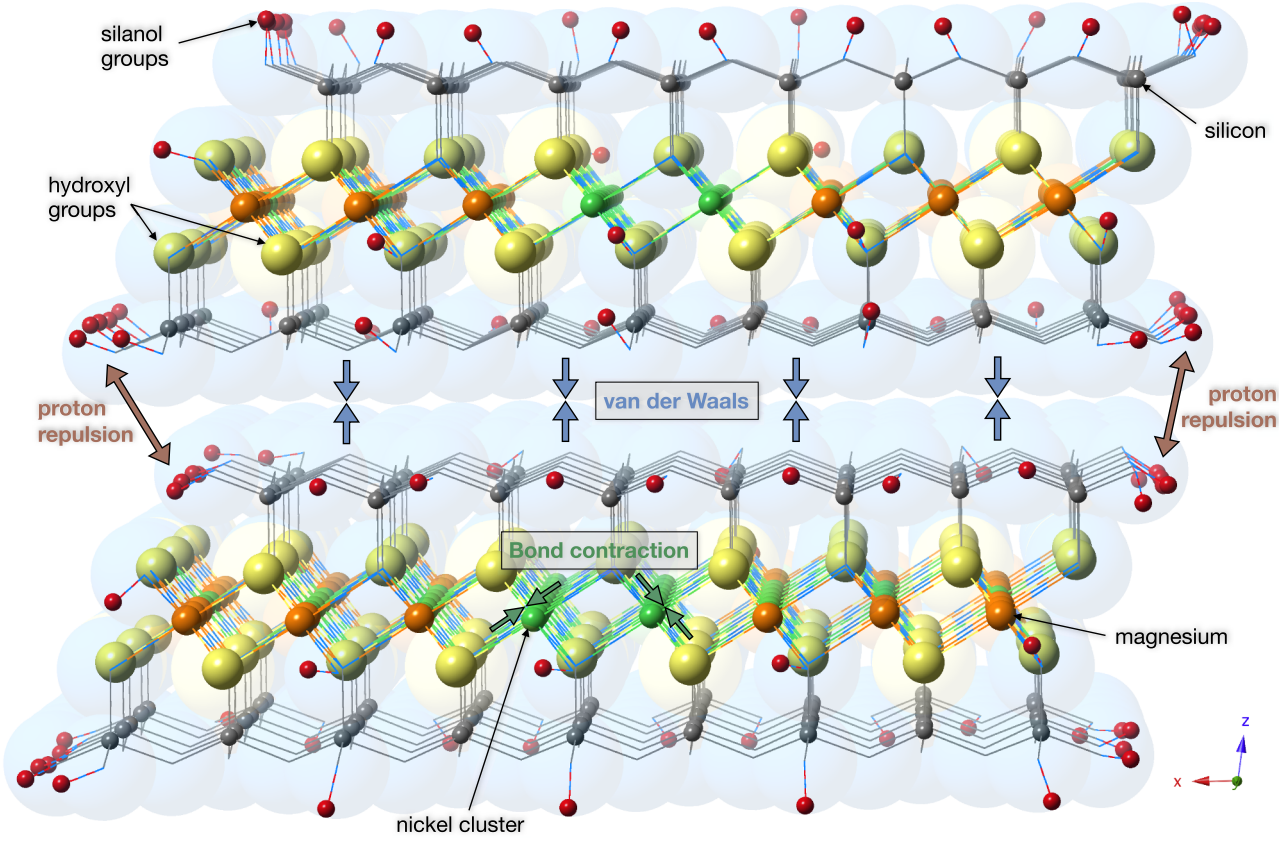

Fig. 9. Molecular model of talc restricted to 20 Å in size in all directions, and including passivating hydrogens (in red) required preserving electro-neutrality. The bonding of passivating hydrogens was relaxed, relative to a fixed TOT structure, using the Monte Carlo molecular dynamics module of CrystalMaker® software, highlighting proton-proton repulsion in the interfoliar space. (For interpretation of the references to color in this figure legend, the reader is referred to the web version of this article.)

approach coupling in situ measurements (optical microscope, EPMA, Raman and XANES) with molecular dynamics relaxation of the passivating protons. It is worth noting that the presence of silanol groups in a large quantity at the edges of the nano-crystals considerably favors the adsorption of water at the crystal surface, especially at high pH as for the saprolite levels (i.e., typically in the pH range 8.5–9.5 as discussed hereafter), and with potentially several water layers (Nawrocki, 1997). However, this adsorbed water is extremely sensitive to the temperature and to vacuum (regarding EPMA technique for example), and most of the in situ analytical techniques (i.e., electron, laser or synchrotron probes), likely cause instantaneous irreversible beam damages. This likely explains that no adsorbed molecular water is observed by Raman spectroscopy.

4.2. Mineral process for nickel enrichment in the saprock horizon

4.2.1. Prerequisites of literature for the understanding of nickel accumulation

Nickel ore deposits in saprolite horizons have been extensively described by many authors, either in New Caledonia (e.g., Cathelineau et al., 2016; Cathelineau et al., 2017; Pelletier, 1996; Troly, 1979; Wells et al., 2009), or in other ore deposits worldwide (e.g., Tauler et al., 2009; Villanova-de-Benavent et al., 2014; Villanova-de-Benavent et al., 2017). The occurrence of phyllosilicate Ni-rich minerals that belong to the serpentine and the talc species at large, is consensual, although questioning about the crystal chemistry of these phases remained (see previous section in this discussion). Two types of ores are generally described at the bottom of regoliths. The first one, the so-called garnierite, which was historically mined in New Caledonia, consists of high grade Ni ore mineralizations that form in open fractures likely initiated at a geological period where the lateritic profiles were poorly developed (Cathelineau et al., 2017; Fritsch et al., 2016; Villanova-de-Benavent et al., 2014), possibly because of well different thermal regimes shortly after the establishment of ophiolitic systems. The second one mainly related to actual supergene processes, is much more homogeneous and diffuse within saprolitic horizons. It represents the current Ni ore that is mined in New Caledonia with a typical cut-off grade of about 2 wt%. However, only a few studies focus on the processes, i.e., driving-forces and mineral reactions, that lead to the concentration of nickel in such saprolitic horizons.

From a thermodynamic approach, Galí et al. (2012) demonstrate that the precipitation of garnierite (i.e., type 1 ore) is characterized by a succession of mineral phases progressively enriched in nickel, where secondary Ni-serpentines crystallize first, followed by Ni-kerolite and possibly Ni-sepiolite minerals. They consider this type 1 nickel ore as an intimate intermixing of three Mg-Ni phyllosilicate solid solutions: serpentine-nepouite, kerolite-pimelite, and sepiolite-falcondoite. In relation with type 2 Ni ore formation, the same authors propose, as an efficient mechanism for Ni supergene enrichment, that congruent dissolution of Ni-poor primary minerals occurs, followed by equilibrium precipitation of Ni-rich secondary phyllosilicates. Dublet et al. (2012) support this hypothesis by showing that, following supergene weathering, Ni is mainly incorporated in secondary phyllosilicates and iron oxyhydroxides in the saprolite (also supported by Domènech et al., 2017). However, no distinction could be made regarding the different phyllosilicate minerals potentially present.

In terms of weathering process, Bucher et al. (2015) bring insights regarding the fluid transport through the regolith profile. These authors suggest that water is efficiently transported via a capillary process to the reaction front, where present-day low-temperature serpentinization

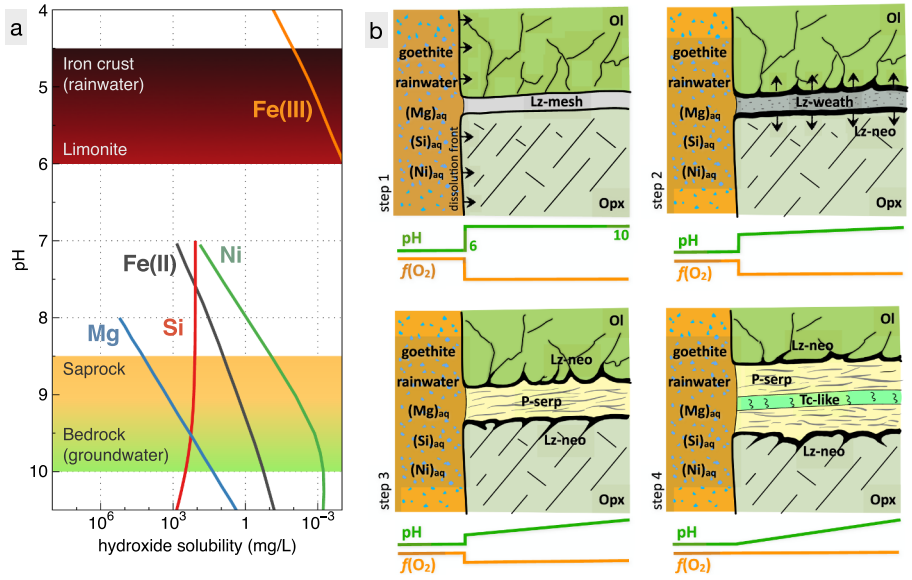

Fig. 10. a) Hydroxide solubility as a function of pH for $Fe(OH)_2$, $Fe(OH)_3$, $Mg(OH)_2$, $Ni(OH)_2$ species (Dyer et al., 1998), labelled Fe(II), Fe(III), Mg, Ni, respectively, and for $Si(OH)_4$ obtained from amorphous silica dissolution; labelled Si (Milne et al., 2014). b) Model for the formation of nickel-bearing minerals in the saprock horizon of the regolith profiles of New Caledonia (inspired by the mineral vein detailed in Fig. 6).

is an active process: the progression of the weathering front is first controlled by reaction kinetics, and then by the transport of fluids. However, if such a process may explain the progression of the weathering front in a saprolitic boulder, it cannot explain the considerable Ni enrichment observed in secondary phyllosilicates. Similarly to our observations at the scale of a boulder, Cathelineau et al. (2016) detailed concentric zoning in large blocks of rock observed in the saprolitic level of the Koniambo massif in New Caledonia. This zoning is composed, from the external to the internal part of the bloc, of 1) a highly oxidized zone, 2) an outer green rim composed of pimelite, 3) an inner white zone, mainly composed of kerolite. They suggest that such a concentric zoning may result from an evapo-precipitation process related to alternate periods of hydration and drying, induced by water table movements. According to the latter authors, such variations in terms of relative humidity could lead to a chromatographic effect, and finally to a mineral zoning and the Ni-Mg segregation. However, no physico-chemical criteria are put forward to explain such a phenomenon.

Finally, in agreement with previous observations, Villanova-de-Benavent et al. (2017) suggest that Ni enrichment in serpentine minerals occurs under supergene conditions, and argue that serpentinization under atmospheric pressure and temperature is thermodynamically supported. According to these authors, pH and Eh are the parameters that control the more significantly the Ni enrichment process. Notably, the stability field of serpentine minerals is shown to significantly increase under oxidizing conditions. In addition, Myagkiy et al. (2017) clearly demonstrate the effect of the vertical progression of the pH front to explain, 1) thickening of the iron-crust located at the top of the regolith profile, and 2) the vertical mobility of the elements, controlling Ni enrichment in saprock horizons. According to these authors the incoming aqueous solution (i.e., rainwater) at equilibrium with atmospheric CO_2 lead to an initial pH of 5.6, while it is likely to decrease to ~4 in the iron crust, to range between 7 and 9 in the saprolite, and to reach 9 to 10 for water at equilibrium with ultrabasic rocks of the bedrock (see also Barnes et al., 1978; Cathelineau et al., 2016 and references therein).

4.2.2. Model for the formation of nickel-bearing minerals

Based on the previous studies exposed above, it comes out that the main causes that lead to nickel accumulation and its mineral sequestration in saprolitic horizons is, beyond the overall *per descensum* context, 1) the relative humidity involving seasonal water table variations under subtropical latitudes (Cathelineau et al., 2016), 2) the high pH steady state disequilibrium (Myagkiy et al., 2017), and 3) the high contrasts of Eh, and therefore fO_2, observed between the surface and the bedrock (Villanova-de-Benavent et al., 2017).

In the present work, we focused our efforts in characterizing a saprolite boulder that typically reflects the first (i.e., actual) stages of bedrock weathering, showing a clear alteration gradient between the inner part, preserved from supergene weathering, and the outer part showing an intense supergene weathering. We coupled chemical analyses, to mineralogical, textural and spectroscopic observations, including accurate iron redox quantification in phyllosilicates and more specifically in Ni-bearing serpentines. We show that Fe^{3+}/Fe_{total} ratios progressively increase in phyllosilicate minerals, from about 0.45 in the internal "fresh" peridotite, to about 0.95 in the external zone of the boulder (Fig. 8). This means that iron redox in phyllosilicate minerals is an excellent proxy to the weathering degree, and traduces a progressive increase of the oxygen fugacity through the phyllosilicate network. This network grows from the external zone at the expense of both, the primary lizardite network (Fig. 3), and the other primary minerals (Fig. 6).

As previously discussed, it has been demonstrated that strong variations of pH occur through the regolith profile, and controls at first order Ni enrichment (Myagkiy et al., 2017). The main pH front is located in the saprock horizon showing an important and steep pH gradient. Then, it should certainly be considered that pH disequilibrium is present at all scales in the regolith. In particular between the outside of the boulder, where the bedrock has been completely dissolved and the mineralogy is largely dominated by iron oxyhydroxides favoring low pH, and the inside of the boulder dominated by ultramafic minerals, favoring high pH.

On this basis, and in order to better understand the behavior of the different cations in such an intense pH gradient, Fig. 10a summarizes the cation hydroxide solubility as a function of pH for ferrous and ferric iron, silicon, magnesium and nickel. Although the presence of CO_3^{2-} (in equilibrium with atmospheric CO_2) or Cl^- in fluids (Barnes et al., 1978) may potentially affect the speciation of the dissolved species, such an approach based on hydroxide solubilities allows to describe, at first order, the behavior of the different cations in the saprock horizon, as exposed hereafter. The black-to-red horizontal band indicates typical pH values for the iron crust and the limonite horizons, respectively. On the other hand, the yellow-to-green band indicates pH values that correspond to the saprolite and the bedrock horizons, respectively. These data show that ferrous iron solubility is decreasing with increasing pH. This will tend to transport iron from the bedrock (or the internal part of the boulder) to the saprolite where its solubility is higher. However, the high oxygen fugacity will oppose to this reaction

by oxidizing ferrous iron into ferric iron for which the solubility is negligible (apart for the very low pH as observed in the iron crust). Therefore, ferric iron is likely to remain in newly formed phyllosilicates, or better precipitate into oxyhydroxide forms such as ferrihydrite or goethite in the saprolite.

Regarding major elements, one can observe that the solubility of Si slightly increases with increasing pH, favoring thus the dissolution of primary silicate minerals in the bedrock. In contrast, the solubility of Mg strongly decreases with increasing pH, and both Si and Mg curves crosscut at around pH 9.5. Such a reversal in the solubility of these two species induces a better ability of the Mg-rich minerals close to hydroxide compounds (such as serpentine, about 26 wt% Mg against 20 wt% Si) to precipitate or crystallize at a pH > 9.5 in close association with ultramafic rocks, while minerals more enriched in Si (such as talc, about 19 wt% Mg for 30 wt% Si) are likely favored below pH 9.5.

Finally, the solubility curve of nickel, although lower than that of ferrous iron above pH 8, shows an intense variation in the pH range comprised between 8 and 10, where a strong solubility decrease is observed for increasing pH. At first order, this means that nickel is more likely to precipitate at higher pH, in close association with ultramafic bedrock, when its solubility is minimum. However, put in perspective with the solubility curves of Mg and Si described above, it actually suggests that serpentine-like minerals, forming at pH > 9.5, will integrate less dissolved nickel. In contrast, talc-like minerals, forming at pH < 9.5, will potentially integrate much more dissolved nickel. This is perfectly consistent with our observations, in the external zone of the boulder, relative to the polygonal serpentine containing about 5 wt% of NiO, and the talc-like containing up to 36 wt% NiO (see Table 2 and Fig. 6).

Fig. 10b proposes a model for the formation of Ni-mineralization during the weathering of the external part of the boulder, which summarizes petrological, mineralogical and chemical observations, in regard to the effects of pH and fO_2 during the weathering of the bedrock, at the saprolite level. The scheme is inspired by the mineralized vein detailed in Fig. 6. The starting assumption is that the bedrock is in contact with weathered, oxidized and acidic materials composed of iron oxyhydroxides (mainly goethite) and rainwater that contains dissolved aqueous species such as $(Mg)_{aq}$, $(Si)_{aq}$, and $(Ni)_{aq}$. One have to distinguish the chemical reactions that occur in contact with external material (i.e., the dissolution front), from the mineralogical reactions that occur inside, from the interaction between external aqueous fluids and primary and subsequent silicate minerals.

The step 1 illustrates the initial stage corresponding to the ultramafic bedrock serpentinized prior supergene events. It represents a lizardite vein developed at the limit between an olivine and an orthopyroxene grain. This lizardite, likely formed during high temperature events of the ophiolite massif (Ulrich et al., 2010), is well crystallized and presents a typical mesh texture (Fig. 4a and b). At this stage, the pH outside the boulder is likely about 6 and the oxygen fugacity quite high, while in the bedrock, the pH is likely about 10 and oxygen fugacity much lower. pH and fO_2 curves show a clearly marked step function between the external and internal part of the rock.

In step 2, the initial lizardite network is fully reused by external fluids that diffuse pervasively. In doing this, the mesh lizardite most likely recrystallizes at low temperature as nanometer-sized lizardite crystals (Lz-weath). This is supported by the isotropic optical properties highlighted in Fig. 4c and d. However, this lizardite does not present significant Ni-enrichment. Although the pH is slowly decreasing because of a progressive re-equilibration with external conditions, it is too high to present significant concentrations in nickel. On the other hand, the oxidation state of iron contained in this lizardite starts increasing up to 60–70% of total iron. This clearly supports an interaction with external fluids as well as an increase of the oxygen fugacity. From this stage, in which external fluids start penetrating pervasively pre-existing serpentine network, a low-temperature serpentinization process occurs by reaction with surrounding olivine and pyroxene to form an in situ lizardite (i.e., Lz-neo, in black in Fig. 10b). Note that Lz-neo shows slight chemical differences as it develops near olivine or orthopyroxene (see, respectively, the chemical compositions of Lz-oliv and Lz-neo in Table 2). These reactions keep going on until the latest stages of the weathering, leading to a strong enlargement of initial veins, before the dissolution front destabilizes the whole.

In step 3, pH keep decreasing close to external part, so that more nickel is available in the aqueous solution when newly formed Mg-serpentine precipitates (i.e., the polygonal serpentine; P-serp); nickel concentration reaches about 5 wt% NiO. Such a decrease in pH is accompanied by a strong increase in fO_2 leading to an increased oxidation of iron in P-serp, up to 95% of ferric iron relative to total iron. As for Lz-weath, the occurrence of nano-sized particles for P-serp is supported by the almost “amorphous” characteristics deduced from isotropic optical properties (Fig. 4e and f). As suggested in Fig. 6h, P-serp formation most likely results from the interaction between external fluids and Lz-neo, which is gradually consumed as it is formed. Note that two types of polygonal serpentine were identified based on small differences in chemical compositions (Table 2) – not represented in Fig. 10b – as they develop either close to olivine or orthopyroxene (Fig. 6). This supports the fact that Lz-neo first develops from olivine or orthopyroxene, and is then remobilized to form P-serp.

In the last step, pH into the vein keep decreasing close to the dissolution surface, while the internal part is still close to 10, resulting in a strong pH gradient. Such a low pH in the external part of the boulder makes Si less soluble than Mg (Fig. 10a). This favors the precipitation of phyllosilicates enriched in Si such as talc-like (described in Fig. 6), instead of the polygonal serpentine which now develops in more internal part, under slightly higher pH. In the same time, Ni solubility strongly increases, which makes it much more available during the precipitation of talc-like minerals. The isocon diagram (i.e., zone 3 vs. zone 1; Fig. 5) demonstrates an outside contribution for nickel. The main talc-like vein described in Fig. 6c contains about 36 wt% NiO (i.e., Tc-like2). However, fortunately some previous residual talc-like remains in the same vein, showing a nickel concentration of about 20 wt% NiO (i.e., Tc-like1; Fig. 6f). This suggests that this vein is fully open to external fluids, in which the fO_2 and pH are almost in equilibrium with the outside. Tc-like1 precipitates first, while the solubility of Ni is less, and the solubilities of Mg and Si almost equilibrate (slightly below pH 9.5 in Fig. 10a). Then at lower pH, the solubilities of Mg and Ni both decrease, but with about 4 orders of magnitude between them. As a result, Mg is mainly leached, while Ni replaces it in the talc-like structure. Such a Mg-to-Ni substitution is all the easier as the talc-like particles are nanometer-sized and strongly hydrophilic (see previous section about crystal chemistry). In the final stage, highest Ni concentrations are observed in Tc-like2 mineral phase. Saprock horizon therefore acts as a chemical trap, which leads to the formation of different generations of Ni-talk-like replacing each-other, and resulting in a progressive increase of the Ni-content (from 20 to 36 wt% NiO in our case). Note that the two generations of talc-like are not represented in Fig. 10b.

The next step most likely corresponds to the progression of the dissolution front, at low pH and high fO_2. It was demonstrated that goethite formation has a potential for hosting part of the available Ni in significant amounts (up to ~25%) in saprolite horizons, while most of the nickel is hosted by phyllosilicate minerals (Dublet et al., 2012). According to the latter study, no distinction could be made between serpentine-like and talc-like Ni-carriers, so that the Ni-bearing phase was called “serpentine” in a very broad sense. However based on our model, although talc-like is present to a lesser extent than polygonal serpentine, it contains much more nickel and is about to be more stable under acidic conditions. As a conclusion, the main Ni-bearing mineral present in the nickel ores of today-mined saprock horizons, is most likely to be talc-like of nano-sized-willemseite type (see Fig. 9), although the presence of Ni-bearing polygonal serpentine cannot be excluded.

5. Conclusions

In this study, we aimed at better understanding the nature and crystal chemistry of the main Ni-bearing minerals in saprock horizons of New Caledonia regoliths, as well as the main mineral processes responsible for their formation. To achieve this goal, we performed a detailed petrological, mineral and chemical characterization of a boulder sampled in the saprock facies of the Koniambo massif (New Caledonia). Thus this study focuses on the Ni concentration processes in saprock horizons, which constitute today the main Ni ore mined in New Caledonia. The approach proposed is a continuous multi-scale study including, 1) the outcrop scale (meter): sampling representative of saprock horizons, 2) the boulder scale (decimeter-to-centimeter): stereo microscope observations, chemical imaging, 3) the thin section scale (millimeter-to-micrometer): optical microscope, chemical analysis and mapping. In addition, spectroscopic measurements allow deriving information at the nanometer scale. Integrating such a large data set leads to the following conclusions:

- First, regarding the crystal chemistry, the main Ni-bearing phyllosilicate species are either polygonal serpentine or talc-like minerals. Concentrations in nickel are more important for talc-like than for polygonal serpentine. Both minerals are poorly crystalline, characterized by i) almost isotropic optical properties, ii) the lack of molecular water in their structure, iii) Ni clustering in their octahedral structural layers, iv) the formation under high fO_2 conditions that leads to ~95% of ferric iron over total iron in polygonal serpentine. In addition, chemical analyses show that both types of minerals systematically contain a large excess of hydroxyls (up to twice the nominal amounts), which can be explained by hydrogen passivation of nano-sized particles forming mainly silanol groups at the crystal edges. According to this model, a direct link can be made between the “water” excess and the particle size in the *ab* crystallographic plane.
- Second, with respect to the processes that lead to over-concentration of nickel in saprolites, reasoning is developed on the basis of the pH versus hydroxide solubility of the main components involved (i.e., iron, magnesium, silicon and nickel), in relation to mineralogy and texture observations. We demonstrate a complete reuse of previous serpentine network for the circulation (pervasive diffusion) of supergene fluids. Then, chronologically, as the pH decreases in the phyllosilicate network, we show the formation of, i) the weathering and oxidation of the primary lizardite network, ii) a newly formed lizardite, resulting from low-temperature interactions between supergene fluids and primary minerals, and participating in the enlargement of phyllosilicate silicate veins, iii) a Ni-rich polygonal serpentine that form at the expense of proximal lizardite, iv) the formation of successive generations of Ni-rich talc-like minerals. Thus, we suggest that the main driving force leading to such chronological succession of minerals is the pH gradient, probably present at all scales: along the vertical regolith profile, and between the inner and outer part of boulders in saprolite horizons.

Supplementary data to this article can be found online at https://doi.org/10.1016/j.gexplo.2018.12.007.

Acknowledgments

We wish to thank Denis Testemale (Institut Néel, ESRF - FAME, Grenoble, France) and Valérie Reita (Institut Néel, Grenoble, France) for their support for Raman spectroscopy. We also thank Valentina Batanova and Valérie Magnin for their precious help, accurate calibration and data collection using the electron probe micro-analysis at ISTerre (UGA, Grenoble, France). We also want to thank François-Xavier Masson, former Master student at ISTerre in 2013 (UGA, Grenoble, France), who participated in the preparation of the boulder sample, and Clément Bonnet for stimulating and relevant discussions during his License internship in Geosciences Montpellier (France) in 2018. Finally we warmly thank both anonymous reviewers for their positive and constructive comments. This research did not receive any specific grant from funding agencies in the public, commercial, or not-for-profit sectors.

References

Andreani, M., Muñoz, M., Marcaillou, C., Delacour, A., 2013. µXANES study of iron redox state in serpentine during oceanic serpentinization. Lithos 178, 70–83.
Auzende, A.-L., Daniel, I., Reynard, B., Lemaire, C., Guyot, F., 2004. High-pressure behaviour of serpentine minerals: a Raman spectroscopic study. Phys. Chem. Miner. 31, 269–277.
Barnes, I., O'Neil, J.R., Trescases, J.J., 1978. Present day serpentinization in New Caledonia, Oman and Yugoslavia. Geochim. Cosmochim. Acta 42, 144–145.
Blanchard, M., Méheut, M., Delon, L., Poirier, M., Micoud, P., Le Roux, C., Martin, F., 2018. Infrared spectroscopic study of the synthetic Mg-Ni talc series. Phys. Chem. Miner. 86, 1321.
Brand, N.W., Butt, C.R.M., Elias, M., 1998. Nickel laterites: classification and features. J. Aust. Geol. Geophys. 17, 81–88.
Brindley, G.W., Hang, P., 1972. The hydrous magnesium-nickel silicate minerals (so-called garnierites). In: International Clay Conference, pp. 41–50.
Brindley, G.W., Maksimovic, Z., 1974. The nature and nomenclature of hydrous nickel-containing silicates. Clay Miner. 10, 271–277.
Brindley, G.W., Bish, D.L., Wan, H., 1979. Compositions, structures, and properties of nickel-containing minerals in the kerolite-pimelite series. Am. Mineral. 64, 615–625.
Bucher, K., Stober, I., Müller-Sigmund, H., 2015. Weathering crusts on peridotite. Contrib. Mineral. Petrol. 169, 1–15.
Butt, C.R.M., Cluzel, D., 2013. Nickel laterite ore deposits: weathered serpentinites. Elements 9, 123–128.
Carignan, J., Hild, P., Mevelle, G., Morel, J., Yeghicheyan, D., 2001. Routine analyses of trace elements in geological samples using flow injection and low pressure on-line liquid chromatography coupled to ICP-MS: a study of geochemical reference materials BR, DR-N, UB-N, AN-G and GH. Geostand. Geoanal. Res. 25, 187–198.
Cathelineau, M., Caumon, M.-C., Massei, F., Brie, D., Harlaux, M., 2015. Raman spectra of Ni-Mg kerolite: effect of Ni-Mg substitution on O-H stretching vibrations. J. Raman Spectrosc. 46, 933–940.
Cathelineau, M., Quesnel, B., Gautier, P., Boulvais, P., Couteau, C., Drouillet, M., 2016. Nickel dispersion and enrichment at the bottom of the regolith: formation of pimelite target-like ores in rock block joints (Koniambo Ni deposit, New Caledonia). Mineral. Deposita 51, 271–282.
Cathelineau, M., Myagkiy, A., Quesnel, B., Boiron, M.-C., Gautier, P., Boulvais, P., Ulrich, M., Truche, L., Golfier, F., Drouillet, M., 2017. Multistage crack seal vein and hydrothermal Ni enrichment in serpentinized ultramafic rocks (Koniambo massif, New Caledonia). Mineral. Deposita 52, 945–960.
Cluzel, D., Aitchison, J.C., Picard, C., 2001. Tectonic accretion and underplating of mafic terranes in the Late Eocene intraoceanic fore-arc of New Caledonia (Southwest Pacific): geodynamic implications. Tectonophysics 340, 23–59.
Debret, B., Andreani, M., Muñoz, M., Bolfan-Casanova, N., Carlut, J., Nicollet, C., Schwartz, S., Trcera, N., 2014. Evolution of Fe redox state in serpentine during subduction. Earth Planet. Sci. Lett. 400, 1–13.
Domènech, C., Galí, S., Villanova-de-Benavent, C., Soler, J.M., Proenza, J.A., 2017. Reactive transport model of the formation of oxide-type Ni-laterite profiles (Punta Gorda, Moa Bay, Cuba). Mineral. Deposita 52, 993–1010.
Dublet, G., Juillot, F., Morin, G., Fritsch, E., Fandeur, D., Ona-Nguema, G., Brown Jr., G.E., 2012. Ni speciation in a New Caledonian lateritic regolith: a quantitative X-ray absorption spectroscopy investigation. Geochim. Cosmochim. Acta 95, 119–133.
Dumas, A., Martin, F., Le Roux, C., Micoud, P., Petit, S., Ferrage, E., Brendlé, J., Grauby, O., Greenhill-Hooper, M., 2013. Phyllosilicates synthesis: a way of accessing edges contributions in NMR and FTIR spectroscopies. Example of synthetic talc. Phys. Chem. Miner. 40, 361–373.
Dumas, A., Mizrahi, M., Martin, F., Requejo, F.G., 2015. Local and extended-order evolution of synthetic talc during hydrothermal synthesis: extended X-ray absorption fine structure, X-ray diffraction, and Fourier transform infrared spectroscopy studies. Cryst. Growth Des. 15, 5451–5463.
Dyer, J.A., Scrivner, N.C., Dentel, S.K., 1998. A practical guide for determining the solubility of metal hydroxides and oxides in water. Environ. Prog. 17, 1–8.
Farges, F., Brown Jr., G.E., Petit, P.-E., Muñoz, M., 2001a. Transition elements in water-bearing silicate glasses/melts. Part I. A high-resolution and anharmonic analysis of Ni coordination environments in crystals, glasses, and melts. Geochim. Cosmochim. Acta 65, 1665–1678.
Farges, F., Muñoz, M., Siewert, R., Malavergne, V., Brown Jr., G.E., Behrens, H., Nowak, M., Petit, P.-E., 2001b. Transition elements in water-bearing silicate glasses/melts. Part II. Ni in water-bearing glasses. Geochim. Cosmochim. Acta 65, 1679–1693.
Fritsch, E., Juillot, F., Dublet, G., Fonteneau, L., Fandeur, D., Martin, E., Caner, L., Auzende, A.-L., Grauby, O., Beaufort, D., 2016. An alternative model for the formation of hydrous Mg/Ni layer silicates (‘deweylite’/‘garnierite’) in faulted peridotites of New Caledonia: I. Texture and mineralogy of a paragenetic succession of silicate infillings. Eur. J. Mineral. 28, 295–311.
Galí, S., Soler, J.M., Proenza, J.A., Lewis, J.F., Cama, J., Tauler, E., 2012. Ni enrichment and stability of Al-free garnierite solid-solutions: a thermodynamic approach. Clay Clay Miner. 60, 121–135.

Grant, J.A., 1986. The isocon diagram - a simple solution to Gresens' equation for metasomatic alteration. Econ. Geol. 81, 1976–1982.
Grant, J.A., 2005. Isocon analysis: a brief review of the method and applications. Phys. Chem. Earth A/B/C 30, 997–1004.
Gresens, R.L., 1967. Composition-volume relationships of metasomatism. Chem. Geol. 2, 47–65.
Manceau, A., Calas, G., 1985. Heterogeneous distribution of nickel in hydrous silicates from New Caledonia ore deposits. Am. Mineral. 70, 549–558.
Manceau, A., Calas, G., 1986. Nickel-bearing clay minerals: II. Intracrystalline distribution of nickel: an X-ray absorption study. Clay Miner. 21, 341–360.
Marcaillou, C., Muñoz, M., Vidal, O., Parra, T., Harfouche, M., 2011. Mineralogical evidence for H2 degassing during serpentinization at 300 °C/300 bar. Earth Planet. Sci. Lett. 303, 281–290.
Mathon, O., Beteva, A., Borrel, J., Bugnazet, D., Gatla, S., Hino, R., Kantor, I., Mairs, T., Muñoz, M., Pasternak, S., Perrin, F., Pascarelli, S., 2015. The time-resolved and extreme conditions XAS (TEXAS) facility at the European Synchrotron Radiation Facility: the general-purpose EXAFS bending-magnet beamline BM23. J. Synchrotron Radiat. 22, 1548–1554.
Merkulova, M., Muñoz, M., Vidal, O., Brunet, F., 2016. Role of iron content on serpentinite dehydration depth in subduction zones: experiments and thermodynamic modeling. Lithos 264, 441–452.
Merkulova, M., Muñoz, M., Brunet, F., Vidal, O., Hattori, K., Vantelon, D., Trcera, N., Huthwelker, T., 2017. Experimental insight into redox transfer by iron- and sulfur-bearing serpentinite dehydration in subduction zones. Earth Planet. Sci. Lett. 479, 133–143.
Milne, N.A., O'Reilly, T., Sanciolo, P., Ostarcevic, E., Beighton, M., Taylor, K., Mullett, M., Tarquin, A.J., Gray, S.R., 2014. Chemistry of silica scale mitigation for RO desalination with particular reference to remote operations. Water Res. 65, 107–133.
Muñoz, M., Bureau, H., Malavergne, V., Ménez, B., Wilke, M., Schmidt, C., Simionovici, A., Somogyi, A., Farges, F., 2005. In situ speciation of nickel in hydrous melts exposed to extreme conditions. Phys. Scr. T115, 921.
Muñoz, M., De Andrade, V., Vidal, O., Lewin, E., Pascarelli, S., Susini, J., 2006. Redox and speciation micromapping using dispersive X-ray absorption spectroscopy: application to iron in chlorite mineral of a metamorphic rock thin section. Geochem. Geophys. Geosyst. 7, Q11020.
Muñoz, M., Pascarelli, S., Aquilanti, G., Narygina, O., Kurnosov, A., Dubrovinsky, L.S., 2008. Hyperspectral μ-XANES mapping in the diamond-anvil cell: analytical procedure applied to the decomposition of (Mg,Fe)-ringwoodite at the upper/lower mantle boundary. High Pressure Res. 28, 665–673.
Muñoz, M., Vidal, O., Marcaillou, C., Pascarelli, S., Mathon, O., Farges, F., 2013. Iron oxidation state in phyllosilicate single crystals using Fe-K pre-edge and XANES spectroscopy: effects of the linear polarization of the synchrotron X-ray beam. Am. Mineral. 98, 1187–1197.
Myagkiy, A., Truche, L., Cathelineau, M., Golfier, F., 2017. Revealing the conditions of Ni mineralization in the laterite profiles of New Caledonia: insights from reactive geochemical transport modelling. Chem. Geol. 466, 274–284.
Nawrocki, J., 1997. The silanol group and its role in liquid chromatography. J. Chromatogr. A 779, 29–71.
Pelletier, B., 1996. Serpentines in nickel silicate ore from New Caledonia. In: Nickel '96. Australasian Institute of Mining and Metallurgy, Melbourne, pp. 197–205.
Pelletier, B., 2003. Les minerais de nickel de Nouvelle-Calédonie. Géologues 138, 30–38.
Perdikatsis, B., Burzlaff, H., 1981. Strukturverfeinerung am Talk Mg3[(OH)2Si4O10]. Z. Krist. 156, 177–186.
Ravel, B., Newville, M., 2005. ATHENA, ARTEMIS, HEPHAESTUS: data analysis for X-ray absorption spectroscopy using IFEFFIT. J. Synchrotron Radiat. 12, 537–541.
Rehr, J.J., Kas, J.J., Vila, F.D., Prange, M.P., Jorissen, K., 2010. Parameter-free calculations of X-ray spectra with FEFF9. Phys. Chem. Chem. Phys. 12, 5503–5513.
Reisner, L.A., Cao, A., Pandya, A.K., 2011. An integrated software system for processing, analyzing, and classifying Raman spectra. Chemom. Intell. Lab. Syst. 105, 83–90.
Rinaudo, C., Gastaldi, D., Belluso, E., 2003. Characterization of chrysotile, antigorite and lizardite by FT-Raman spectroscopy. Can. Mineral. 41, 883–890.
Shannon, R.D., 1976. Revised effective ionic radii and systematic studies of interatomic distances in halides and chalcogenides. Acta Crystallogr. A 32, 751–767.
Solé, V.A., Papillon, E., Cotte, M., Walter, P., Susini, J., 2007. A multiplatform code for the analysis of energy-dispersive X-ray fluorescence spectra. Spectrochim. Acta B At. Spectrosc. 62, 63–68.
Tauler, E., Proenza, J.A., Galí, S., Lewis, J.F., Labrador, M., García-Romero, E., Suarez, M., Longo, F., Bloise, G., 2009. Ni-sepiolite-falcondoite in garnierite mineralization from the Falcondo Ni-laterite deposit, Dominican Republic. Clay Miner. 44, 435–454.
Teo, B.K., 1986. EXAFS: Basic Principles and Data Analysis. Springer Berlin Heidelberg, Berlin, Heidelberg.
Troly, G., 1979. Nickel deposits in New Caledonia: some factors influencing their formation. In: International Laterite Symposium. AIME, New Orlean, pp. 85–119.
Ulrich, M., Picard, C., Guillot, S., Chauvel, C., Cluzel, D., Meffre, S., 2010. Multiple melting stages and refertilization as indicators for ridge to subduction formation: the New Caledonia ophiolite. Lithos 115, 223–236.
Ulrich, M., Muñoz, M., Guillot, S., Cathelineau, M., Picard, C., Quesnel, B., Boulvais, P., Couteau, C., 2014. Dissolution–precipitation processes governing the carbonation and silicification of the serpentinite sole of the New Caledonia ophiolite. Contrib. Mineral. Petrol. 167, 952.
Villanova-de-Benavent, C., Proenza, J.A., Galí, S., García-Casco, A., Tauler, E., Lewis, J.F., Longo, F., 2014. Garnierites and garnierites: textures, mineralogy and geochemistry of garnierites in the Falcondo Ni-laterite deposit, Dominican Republic. Ore Geol. Rev. 58, 91–109.
Villanova-de-Benavent, C., Domènech, C., Tauler, E., Galí, S., Tassara, S., Proenza, J.A., 2017. Fe-Ni-bearing serpentines from the saprolite horizon of Caribbean Ni-laterite deposits: new insights from thermodynamic calculations. Mineral. Deposita 52, 979–992.
Wells, M.A., Ramanaidou, E.R., Verrall, M., Tessarolo, C., 2009. Mineralogy and crystal chemistry of “garnierites” in the Goro lateritic nickel deposit, New Caledonia. Eur. J. Mineral. 21, 467–483.
Wilke, M., Farges, F., Petit, P.-E., Gordon, E., Brown, J., Martin, F., 2001. Oxidation state and coordination of Fe in minerals: an Fe K-XANES spectroscopic study. Am. Mineral. 86, 714–730.